Research Square

Preprints are preliminary reports that have not undergone peer review.
They should not be considered conclusive, used to inform clinical practice,
or referenced by the media as validated information.

In vivo base editing rescues hearing in humanized MPZL2 mice within a structure-dependent therapeutic window

Sang-Yeon Lee

maru4843@hanmail.net

Seoul National University Hospital https://orcid.org/0000-0003-3566-8708

Sangsu Bae

Seoul National University College of Medicine https://orcid.org/0000-0003-3615-8566

Sohyang Jeong

Department of Otorhinolaryngology-Head and Neck Surgery, Seoul National University Hospital, Seoul National University College of Medicine, Seoul, Republic of Korea https://orcid.org/0009-0005-7312-0008

Byeong-Hee Kang

Seoul National University Hospital

Won Hoon Choi

Seoul National University Hospital

Yeji Choi

Seoul National University Hospital

Hansol Koo

Cancer Research Institute, Seoul National University College of Medicine, Seoul 03080, Republic of Korea

Woo Seok Byun

Handong Global University https://orcid.org/0000-0002-4837-6563

Yejin Yun

Seoul National University https://orcid.org/0000-0002-0719-9599

Sung Ho Jung

Department of Otorhinolaryngology-Head and Neck Surgery, Seoul National University Hospital, Seoul National University College of Medicine, Seoul, Republic of Korea

Juhye Choi

Seoul National University Hospital

Chanju Jung

Seoul National University College of Medicine

Dong Woo Nam

Seoul National University Hospital https://orcid.org/0000-0002-2350-6077

Heeyoung Seok

Department of Transdisciplinary Research and Collaboration, Genomics Core Facility, Biomedical Research Institute, Seoul National University Hospital, Seoul, Republic of Korea

Seunghee Cho

AAVATAR Therapeutics

Sung-Yeon Lee

Macrogen Inc.

Article

Keywords:

Posted Date: September 16th, 2026

DOI: https://doi.org/10.21203/rs.3.rs-10977804/v1

License: This work is licensed under a Creative Commons Attribution 4.0 International License. Read Full License

Additional Declarations: There is **NO** Competing Interest.

In vivo base editing rescues hearing in humanized *MPZL2* mice within a structure-dependent therapeutic window

Sohyang Jeong[1#], Byeong-Hee Kang[1#], Won Hoon Choi[1#], Yeji Choi[1#], Hansol Koo[2#], Woo Seok Byun[1], Yejin Yun[1], Sung Ho Jung[1], Juhye Choi[1], Chanju Jung[3], Dong Woo Nam[1], Heeyoung Seok[4], Seunghee Cho[5], Sung-Yeon Lee[6,7], Sangsu Bae[2,3,8]*, Sang-Yeon Lee[1,9]*

[1]Department of Otorhinolaryngology-Head and Neck Surgery, Seoul National University Hospital, Seoul National University College of Medicine, Seoul, Republic of Korea.

[2]Cancer Research Institute, Seoul National University College of Medicine, Seoul 03080, Republic of Korea.

[3]Department of Biomedical Sciences, Seoul National University College of Medicine, Seoul 03080, South Korea

[4]Department of Transdisciplinary Research and Collaboration, Genomics Core Facility, Biomedical Research Institute, Seoul National University Hospital, Seoul, Republic of Korea

[5]AAVATAR Therapeutics, 12925, Gyeonggi-do, Republic of Korea.

[6]GEM Division, Macrogen Inc., Seoul, South Korea, 07573.

[7]Laboratory of Theriogenology, College of Veterinary Medicine, Seoul National University, Seoul, South Korea, 08826.

[8]Genomic Medicine Institute, Seoul National University College of Medicine, Seoul 03080, Republic of Korea.

[9]Sensory Organ Research Institute, Seoul National University Medical Research Center, Seoul, Republic of Korea.

[#]These authors contributed equally.

*To whom correspondence should be addressed to S-Y.L. (maru4843@hanmail.net) and S.B. (sbae7@snu.ac.kr)

Abstract

In vivo base editing is advancing toward clinical translation for hereditary deafness, yet efficacy has been established almost exclusively after neonatal intervention, a stage corresponding to human mid-gestation. Whether correction remains effective in a mature, progressively degenerating cochlea, and what sets the limits of such intervention, remain unresolved. We generated a full-length humanized mouse model carrying the *MPZL2* c.220C>T East Asian founder variant (FL-*hMPZL2*$^{Q74X/Q74X}$), which reproduced patient-derived nonsense-mediated decay and recapitulated the natural history of DFNB111, revealing a sequential pathology in which Deiters' cell (DC) disorganization precedes DC–outer hair cell (OHC) degeneration. Using a dual-adeno-associated virus (AAV)-ie-K558R system encoding PAM-flexible ABE8eWQ–SpRY, we treated mice after hearing onset and, subsequently, after cochlear maturation. When DC architecture remained intact, treatment durably improved low- to mid-frequency hearing, restored *MPZL2* expression, delayed DC disorganization, preserved DC and OHC survival, and shifted DC-associated transcriptional programs toward a wild-type-like state. Once DC disorganization emerged, treatment conferred no benefit despite comparable on-target editing. Extracochlear editing was minimal, with no organ toxicity, cytotoxicity, or inflammatory responses in human cells. Therefore, base editing remains effective after cochlear maturation in *MPZL2*-associated DFNB111, with the therapeutic window bounded by cochlear structural integrity rather than chronological age or editing competence.

Introduction

Hereditary deafness is a common sensory disorder, with pathogenic variants identified in more than 150 genes[1]. Adeno-associated virus (AAV)-mediated gene augmentation has restored auditory function in preclinical models of *OTOF*, *GJB2*, *SLC26A4*, *STRC*, *USH1C*, *MPZL2*, and *TMC1*[2,3,4,5,6,7,8]. Clinical translation has advanced most decisively for *OTOF*-associated hearing loss, culminating in the 2026 FDA approval of Otarmeni, the first gene therapy approved for hereditary deafness[9,10]. These advances establish inner-ear gene therapy as a clinically viable modality.

Since the adaptation of CRISPR–Cas9 for genome editing[11,12], base editors have enabled precise sequence correction[13,14]. Adenine and cytosine base editors enable targeted A•T-to-G•C and C•G-to-T•A transitions, respectively, without generating DNA double-strand breaks (DSBs), thereby reducing the risk of DSB-associated large deletions and chromosomal rearrangements[13,14,15]. Recently, the first patient-specific in vivo base editing for severe carbamoyl-phosphate synthetase 1 deficiency provided early evidence of clinical feasibility[16].

In vivo base editing has restored auditory function in several preclinical models of hereditary deafness[17,18,19]. Among these, *MPZL2* c.220C>T (p.Q74X) is an East Asian founder variant and a major cause of DFNB111, which is characterized by progressive hearing loss, disorganization of Deiters' cell (DC) architecture, and degeneration of the organ of Corti[18,20,21,22]. Unlike deafness genes that compromise cochlear hair cells (HCs) at the earliest stages, *MPZL2* is expressed predominantly in DCs[7,18,20,21], and the associated hearing loss progresses gradually, suggesting that HCs may remain amenable to correction well beyond disease onset. We previously demonstrated that a PAM-flexible adenine base editor corrected *MPZL2* c.220C>T after neonatal inner ear delivery in a humanized cDNA knock-in model[18]. However, because cochlear maturation occurs prenatally in humans but postnatally in mice, neonatal mouse intervention has limited relevance to postnatal clinical treatment[23]. Whether base editing remains effective after cochlear maturation in progressive hearing loss with evolving organ of Corti pathology therefore remained unknown.

Thus, this study generated matched full-length humanized *MPZL2* knock-in mouse models carrying either the c.220C>T variant or the wild-type (WT) allele, each encompassing approximately 15.9 kb of the human *MPZL2* genomic locus. The mutant model recapitulated the c.220C>T-associated nonsense-mediated decay (NMD) observed in patient-derived cells and the progressive hearing loss of DFNB111[24]. Using an optimized dual-AAV-ie-K558R system encoding PAM-flexible ABE8eWQ–SpRY, we first treated mice after hearing onset and then extended treatment to post-maturation stages. Base editing significantly restored auditory function when administered at P28–P30, after auditory impairment had developed but before structural pathology emerged. In contrast, no clear benefit was observed at P42, after DC disorganization had begun, despite comparable on-target editing efficiencies. Treatment also restored *MPZL2* expression, delayed DC disorganization, and shifted DC transcriptional programs toward a WT-like state. Safety analyses showed minimal extracochlear editing and no detectable organ toxicity, inflammation, or cytotoxicity in human cell assays. Together, these findings demonstrate that in vivo base editing can restore auditory function after cochlear maturation and define a disease stage-dependent therapeutic window for *MPZL2* c.220C>T-associated DFNB111.

Results

Generation and molecular characterization of full-length humanized *MPZL2* mouse models

CRISPR–Cas9-mediated homologous recombination was used to generate matched full-length humanized *MPZL2* mouse models (**Fig. 1a**). The endogenous mouse *Mpzl2* locus was replaced with a knock-in fragment of approximately 15.9 kb (GRCh38 chr11:g.118252917-g.118268857) spanning about 5 kb upstream of the human *MPZL2* ATG start codon to 0.5 kb downstream of the 3'-untranslated region (UTR), including all six exons and intervening introns harboring the c.220C>T(p.Q74X) nonsense variant, thereby establishing a full-length humanized *MPZL2* c.220C>T knock-in mouse (FL-*hMPZL2*$^{Q74X/Q74X}$). Correctly targeted embryonic stem cell (ESC) clones were confirmed by Southern blotting using Neo, 5′-arm, and 3′-arm probes (**Supplementary Fig. 1a**); meanwhile, precise insertion of the human *MPZL2* genomic fragment at the endogenous mouse *Mpzl2* locus was further verified by Sanger sequencing across the 5′ and 3′ recombination junctions (**Supplementary Fig. 1b**). A corresponding full-length humanized *MPZL2* WT mouse model (FL-*hMPZL2*$^{WT/WT}$) was then established as a control. Sanger sequencing of genomic DNA confirmed the *hMPZL2*^{Q74X} and *hMPZL2*^{WT} alleles (**Supplementary Fig. 1c**). RT-PCR and sequencing of cDNA amplicons spanning multiple exon junctions and the coding sequence confirmed correct splicing of the humanized *MPZL2* transcript and the associated sequence identity with the human reference transcript (**Supplementary Fig. 1d–e**). We next examined whether the *hMPZL2*^{Q74X} transcript underwent NMD. In P28 cochleae, *MPZL2* transcript abundance in FL-*hMPZL2*$^{Q74X/Q74X}$ mice was reduced to 18.45% ± 0.26% of that in FL-*hMPZL2*$^{WT/WT}$ mice and increased to 76.77% ± 1.57% after cycloheximide treatment, consistent with NMD (**Fig. 1b–c**). Despite this marked reduction, quantitative RT-PCR detected residual c.220C>T transcript, consistent with the previously reported incomplete NMD in an independently generated *Mpzl2*$^{Q74*/Q74*}$ model[7]. Species-specific RT-PCR of P56 cochleae further showed human *MPZL2* expression in FL-*hMPZL2*$^{WT/WT}$ and endogenous mouse *Mpzl2* expression in *Mpzl2* WT mice, whereas the *hMPZL2*^{Q74X} signal was barely detectable in FL-*hMPZL2*$^{Q74X/Q74X}$ cochleae (**Supplementary Fig. 1e**). A similar pattern was observed in patient-derived SNUH422-907 induced pluripotent stem cells (iPSCs) homozygous for *MPZL2* c.220C>T (**Supplementary Fig. 2a–h**). *MPZL2* transcript abundance was similarly reduced to 13.91% ± 0.60% relative to GM25256 control iPSCs[25] and increased to 83.32% ± 4.75% following cycloheximide treatment (**Supplementary Fig. 2i–j**). Consistent with depletion of the c.220C>T transcript, MPZL2 immunoreactivity was undetectable in the organ of Corti of FL-*hMPZL2*$^{Q74X/Q74X}$ mice at P28 and P56 (**Supplementary Fig. 3**). In FL-*hMPZL2*$^{WT/WT}$ mice, MPZL2 protein was expressed throughout the organ of Corti, with particularly prominent enrichment in the phalangeal processes[26,27], basolateral membranes[28], and footplates[29] of DCs, with no discernible difference between P28 and P56. This localization pattern closely resembled that observed in *Mpzl2* WT mice. The antibody used here recognizes both mouse and human MPZL2 in the cochlea[7,18,20,21,22]. Overall, we generated and molecularly validated full-length humanized *MPZL2* mouse models that recapitulate patient-derived c.220C>T-associated NMD.

Age-dependent auditory and cochlear structural phenotypes in FL-*hMPZL2*$^{Q74X/Q74X}$ mice

Next, we assessed whether the FL-*hMPZL2*$^{Q74X/Q74X}$ mouse model reproduced the associated auditory phenotype. Auditory brainstem response (ABR) measurements revealed progressive hearing loss in FL-*hMPZL2*$^{Q74X/Q74X}$ mice. At 4 weeks of age, FL-*hMPZL2*$^{Q74X/Q74X}$ mice exhibited predominantly mild hearing loss, with thresholds worsening to moderate-to-severe levels at high frequencies. By 6 and 8 weeks, hearing loss had progressed to moderate-to-severe levels, with elevated thresholds across the entire frequency range. By 12 weeks, the mice had developed severe-to-profound hearing loss across all tested frequencies (**Fig. 1d**). We next evaluated outer hair cell (OHC) function using distortion product otoacoustic emission (DPOAE), which showed a similar pattern of progressive dysfunction (**Fig. 1e**). FL-*hMPZL2*$^{WT/WT}$ mice showed normal hearing across all tested ages and normal cochlear architecture comparable to that of *Mpzl2* WT mice (**Supplementary Fig. 4a–c**), indicating that the phenotype was associated with the c.220C>T variant rather than humanization of the locus. Thus, to determine the clinical relevance of our model, we compiled *MPZL2* variants classified as likely pathogenic or pathogenic according to ACMG/AMP criteria from ClinVar and our in-house cohort, confirming c.220C>T as the most recurrent pathogenic allele and an East Asian founder variant (**Supplementary Fig. 5a–c**). We then characterized the natural history of c.220C>T-associated hearing loss using 138 published and in-house pure-tone audiograms from 31 affected individuals (**Supplementary Data 1**), revealing progression from mild to severe-to-profound hearing loss over several decades (**Supplementary Fig. 5d**). Compared with our previously reported *hMPZL2*$^{Q74X/Q74X}$ cDNA knock-in model[18], the FL-*hMPZL2*$^{Q74X/Q74X}$ model more faithfully recapitulated the progressive hearing loss trajectory observed in DFNB111 patients harboring the c.220C>T variant, as demonstrated by Pearson correlation coefficient (r = 0.910 vs. 0.733) and cosine similarity (0.956 vs. 0.879) (**Supplementary Fig. 5e–f**).

Subsequently, we examined age-dependent histopathological progression in FL-*hMPZL2*$^{Q74X/Q74X}$ mice using whole-mount immunofluorescence (IF), focusing on OHC and DC numbers and the degree of DC disorganization (**Fig. 1f–g).** Although no overt DC or OHC loss was observed at 4–8 weeks, DC disorganization first appeared at 6 weeks, primarily in the basal turn, and progressed by 8 weeks. By 12 weeks, FL-*hMPZL2*$^{Q74X/Q74X}$ mice exhibited marked DC and OHC loss with a clear base-to-apex gradient, with profound loss in the basal turn and substantial preservation in the mid-apical turns, whereas both OHCs and DCs remained largely intact in *Mpzl2* WT mice (**Fig. 1f–g**). Cross-sectional IF confirmed this basal-turn loss, showing comparable reductions in both OHCs and DCs in FL-*hMPZL2*$^{Q74X/Q74X}$ mice relative to *Mpzl2* WT mice **(Supplementary Fig. 6a–b)**. In contrast, the stria vascularis and spiral ligament remained structurally intact, and spiral ganglion neurons (SGNs) density did not differ significantly between FL-*hMPZL2*$^{Q74X/Q74X}$ and *Mpzl2* WT mice **(Supplementary Fig. 6c–g)**. To quantify age-dependent DC spatial disorganization, we used two complementary metrics: 9-nearest-neighbor (9-NN) distance and the coefficient of variation of 9-NN distance (9-NN CV), previously used to measure three-dimensional (3D)-based cellular dispersion[30], with elevated values indicating worsening DC disorganization (**Fig. 1h–j**). The 9-NN analysis was restricted to regions retaining sufficient DCs for spatial quantification (≥70% of WT-normalized DC counts). At 6 weeks, mean 9-NN distance increased significantly by 31.65% (P = 0.0029) in the basal turn, with a corresponding

33.25% increase in 9-NN CV (P = 0.0273). By 8 weeks, mean 9-NN distance significantly increased by 29.41% (P = 0.0301) and 44.24% (P = 0.0007), whereas 9-NN CV increased by 46.50% (P = 0.0045) and 55.34% (P = 0.0001) in the middle and basal regions, respectively. At 12 weeks, FL-*hMPZL2*$^{Q74X/Q74X}$ mice exhibited marked DC loss in the basal and middle turns (<70% of WT-normalized DC counts), precluding 9-NN quantification. Collectively, these analyses delineate an age-dependent disease trajectory: high-frequency auditory dysfunction with preserved cochlear structure at 4 weeks; DC disorganization emerging predominantly in the basal turn at 6 weeks and progressing by 8 weeks; and overt DC–OHC degeneration with a base-to-apex gradient by 12 weeks.

Dose optimization and selection of the dual-AAV-ie-K558R-ABE8eWQ-SpRY:sgRNA3 system

A previous study showed that AAV-ie-K558R efficiently transduced neonatal cochlear HCs and SCs, with enhanced transduction of OHCs and basal-turn SCs compared with parental AAV-ie[31]. To evaluate AAV-ie-K558R-GFP delivery in the mature inner ear, we developed a modified posterior semicircular canal (PSCC) injection procedure adapted from previously described protocols[32,33] (**Supplementary Movie 1**). Using this approach, we administered AAV-ie-K558R-green fluorescent protein (GFP) to *Mpzl2* WT mice at P14, P28, and P42 (1.5 µL per ear; 5.11 × 10^{13} vg/mL) and examined cochlear GFP expression 7 days later. GFP signals were detected throughout the organ of Corti at all three treatment ages and broadly overlapped with MPZL2 immunoreactivity (**Fig. 2a)**, providing qualitative support for transduction of disease-relevant MPZL2-expressing cells. We packaged ABE8eWQ-SpRY:sgRNA3, which showed the most favorable editing profile in our previous systematic screen targeting *MPZL2* c.220C>T and exhibited minimal bystander or off-target editing in vitro[18], into a dual-AAV-ie-K558R system using a split-intein strategy. We then compared low- and high-titer formulations of the dual-AAV-ie-K558R-ABE8eWQ-SpRY:sgRNA3 to identify a dose that maximized editing efficiency while minimizing safety risks. The low-titer formulation contained 1 × 10^{13} vg/mL of each vector. In contrast, the high-titer formulation contained 5 × 10^{13} and 5.22 × 10^{13} vg/mL of the N- and C-terminal vectors, respectively (**Fig. 2b**). For cell-based comparison, the corresponding formulations were evaluated at low- and high-dose conditions of 1 × 10^{5} and 5 × 10^{5} genome copies per cell, respectively (**Fig. 2c**). Co-delivery of the N- and C-terminal vectors generated full-length reconstituted ABE8eWQ–SpRY, with reconstitution efficiency increasing from 29.05% ± 4.05% under the low-dose to 46.02% ± 3.65% under the high-dose condition (**Fig. 2d and Supplementary Fig. 7**). This increase was accompanied by enhanced editing of the intended A5 target base, rising from 1.44% (low-dose condition) to 10.05% (high-dose condition). In contrast, adenine bystander editing and non-canonical cytosine conversion at C3, C6, and C8 remained minimal under both conditions (**Fig. 2e**). We next assessed guide-dependent off-target editing at five candidate genomic sites selected from our previous screening, identified by GUIDE-seq and Cas-OFFinder[18,34,35]. A-to-G editing frequencies were low at all candidate off-target sites and showed no dose-dependent increase (**Fig. 2f**). Based on these in vitro results, we evaluated the tolerability of the high-titer formulation following P14–P15 inner-ear administration in *Mpzl2* WT mice. ABR thresholds did not differ between treated and uninjected mice at 4, 8, or 12 weeks. OHC and DC survival were likewise preserved, with no detectable treatment-associated toxicity (**Fig. 2g–h and Supplementary Fig. 8**). Collectively, we optimized the dual-AAV-ie-K558R–ABE8eWQ-SpRY:sgRNA3

system for in vivo base editing after hearing onset and cochlear maturation by refining vector dose and injection protocol, achieving efficient mature cochlear delivery, enhanced on-target editing with minimal bystander and off-target editing, and no detectable cochlear toxicity.

In vivo post-hearing-onset editing efficiency and off-target profiling

We next evaluated in vivo editing efficiency in organ of Corti samples harvested at P28–P30 from FL-*hMPZL2*$^{Q74X/Q74X}$ mice treated at P14–P15, after hearing onset. The average editing efficiency at position A5 was 3.92 ± 1.25% (1.20–8.30%). However, A-to-G conversions at adjacent adenine bases remained very low, below 0.2% (**Fig. 2i**). To assess editing-enriched cochlear cell populations, epithelial cells of the organ of Corti were further sorted by fluorescence-activated cell sorting (FACS) using CD326 (EpCAM), an epithelial marker expressed in both HCs and SCs[36]. Targeted deep sequencing of the CD326^{+} sorted population revealed a mean editing efficiency of 29.90 ± 9.24% (3.12–56.16%). To further enrich for HCs within the epithelial population, dissociated cells were additionally pulse-labeled with FM1–43, which enters cochlear HCs through functional mechanotransduction channels[37]. Approximately 3,000 CD326^{+}/FM1–43^{high} cells were collected for sequencing (**Fig. 2j and Supplementary Fig. 9a–b)**, with a mean editing efficiency of 11.47 ± 7.69% (1.01–49.25%) (**Fig. 2k**). HC enrichment achieved by CD326 and FM1–43 gating was further validated by cross-sectional IF and bulk-RNA sequencing (**Supplementary Fig. 9c-f**). Finally, we assessed in vivo DNA and RNA off-target effects. DNA off-target analysis was performed using in vivo treated samples showing on-target editing efficiencies of 1.79%, 4.14%, 8.26% (**Fig. 2l**). Potential off-target sites in the mouse genome were identified using Cas-OFFinder, allowing up to two mismatches in the 19 nt sgRNA target sequence while excluding the additional 5' G introduced for U6-driven transcription. Targeted deep sequencing revealed minimal A-to-G editing at these sites, with all editing rates below 0.2% in the injected cochleae. No significant difference in editing was observed compared to the contralateral, non-injected cochleae. Next, transcriptome-wide RNA off-target effects were assessed by RNA sequencing of paired cochlear tissues from the injected and the contralateral non-injected cochleae as controls. Across the transcriptome, no consistent increase in the number of A-to-I editing events was observed in the injected cochleae compared with the contralateral non-injected cochleae **(Fig. 2m)**. Collectively, these findings demonstrate efficient in vivo editing, with enriched on-target editing in disease-relevant organ of Corti epithelial cell populations and minimal bystander and off-target editing.

Base editing initiated after hearing onset restores auditory function and preserves organ of Corti architecture

A schematic overview of in vivo base editing after hearing onset, followed by auditory and histological assessments, is shown in **Fig. 3a**. Representative click-evoked ABR waveforms at 12 weeks showed restored auditory responses in treated mice compared with untreated FL-*hMPZL2*$^{Q74X/Q74X}$ mice (**Fig. 3b**). Treated ears exhibited significantly lower ABR thresholds than untreated FL-*hMPZL2*$^{Q74X/Q74X}$ ears at 6, 8, and 12 weeks (**Fig. 3c–e; statistical comparisons, Supplementary Table 1**). The significance comprised click and 8–24 kHz at 6 weeks and click and 4–16 kHz at 8 and 12 weeks. The benefit sustained across low-to-mid frequencies, while the 24 kHz benefit lost beyond 6 weeks. The effect was

largest at 8 kHz throughout (all $P \leq 0.0005$), where treated thresholds remained below 40 dB while untreated thresholds exceeded 69 dB by 12 weeks. Likewise, DPOAE thresholds were significantly improved in treated ears at 8 kHz at 8 and 12 weeks and at 16 kHz at 8 weeks, indicating frequency-dependent recovery of OHC function through 12 weeks of age (**Fig. 3f–h**). To determine whether this functional recovery was accompanied by molecular rescue, we quantified *MPZL2* expression in cochleae from P28–P30 mice. Quantitative RT-PCR showed that *MPZL2* transcript abundance in treated FL-*hMPZL2*$^{Q74X/Q74X}$ mice reached 57.38% ± 3.37% of that in age-matched FL-*hMPZL2*$^{WT/WT}$ mice (**Fig. 4a–b**). This partial recovery is consistent with reduced NMD-mediated transcript depletion following correction of the c.220C>T variant. At the protein level, MPZL2 immunoreactivity was broadly restored throughout the organ of Corti in treated ears, including the phalangeal processes, basolateral membranes, and footplates of DCs adjacent to the basilar membrane (**Fig. 4c–d**). Since DC disorganization was the earliest detectable structural pathology, we assessed whether base editing preserved DC organization by quantifying 9-NN distance and 9-NN CV. At 6 weeks, FL-*hMPZL2*$^{Q74X/Q74X}$ mice showed early DC disorganization in the basal turn. Treatment reduced 9-NN distance and 9-NN CV in the basal turn by 18.56% and 23.12%, respectively, relative to untreated mice ($P = 0.0086$ and $P = 0.0118$), corresponding to 77.13% and 92.63% normalization toward WT levels. By 8 weeks, DC disorganization was evident in the basal and middle turns of FL-*hMPZL2*$^{Q74X/Q74X}$ mice. In the basal turn, treatment reduced the 9-NN distance and 9-NN CV by 21.14% and 35.66%, respectively, compared with untreated mice ($P = 0.0086$ and $P = 0.0006$), corresponding to 68.94% and 100.08% normalization toward WT levels. In the middle turn, the 9-NN CV was significantly reduced by 32.37% ($P = 0.0027$), corresponding to 101.89% normalization, whereas the 9-NN distance showed no significant difference (0.43% reduction, $P > 0.9999$; **Fig. 4e–f; statistical comparisons, Supplementary Table 2**). At 12 weeks, FL-*hMPZL2*$^{Q74X/Q74X}$ mice exhibited marked DC loss in the basal and middle turns, precluding 9-NN quantification in the middle and basal turns of untreated mice. Treatment significantly improved DC survival relative to untreated mice in the middle ($P < 0.0001$) and basal ($P < 0.0001$) turns (**Fig. 4g–h**), restoring sufficient DC numbers in the treated middle and basal turns for 9-NN quantification. In the basal turn, 9-NN distance and 9-NN CV were improved but remained significantly higher than WT levels ($P = 0.0084$; $P = 0.0051$; **Fig. 4i–j**), instead approximating those of untreated 6-week-old FL-*hMPZL2*$^{Q74X/Q74X}$ mice with DC disorganization ($P > 0.9999$). Additionally, OHC survival was significantly increased following treatment in the middle ($P = 0.0405$) and basal ($P < 0.0001$) turns. Overall, in vivo base editing after hearing onset restored auditory function and *MPZL2* expression, delayed DC disorganization, and preserved DC and OHC survival.

Post-maturation base editing restores auditory function before the onset of structural pathology

Although in vivo base editing at P14–P15, after hearing onset, was therapeutically effective in FL-*hMPZL2*$^{Q74X/Q74X}$ mice, this stage broadly corresponds to second-trimester cochlear development in humans, limiting its clinical translational relevance[23,38]. To address this translational gap, we extended treatment to P28–P30, after cochlear maturation and at a disease stage characterized by established auditory impairment but largely preserved organ of Corti architecture. A schematic overview of the post-maturation P28–P30 treatment and subsequent longitudinal assessments is shown in **Fig. 5a**. Targeted

deep-sequencing of the organ of Corti showed a mean on-target A5 editing efficiency of 3.46 ± 0.36%, which did not differ from that observed with P14–15 treatment (3.92 ± 1.25%, $P > 0.9999$). Bystander editing at A1, A2, and A9 did not exceed 0.14% (**Supplementary Fig. 10**). Therefore, we next assessed auditory recovery following treatment at P28–30. Treated mice exhibited significantly lower ABR thresholds than untreated FL-*hMPZL2*$^{Q74X/Q74X}$ mice at 8, 12, 16, and 20 weeks (**Fig. 5b–e; Supplementary Table 3**). The significance comprised click and 8–16 kHz at 8 weeks, click and 4–16 kHz at 12 weeks, and click and 4–8 kHz at 16 and 20 weeks. The 16 kHz benefit was marginal at 12 weeks and no longer detected thereafter, whereas the benefit at click and 4–8 kHz was retained at every timepoint. At 8 kHz, the frequency of greatest effect (all $P \leq 0.0009$), the between-group difference reached 22.1 dB at 12 weeks and remained significant through 20 weeks. DPOAE thresholds were significantly improved at 8, 16, and 24 kHz at 8 weeks, with benefits at 8 kHz persisting through 20 weeks (**Fig. 5f–i**). Following P28–P30 treatment, OHC survival at 12 weeks was significantly increased in the basal turn ($P < 0.0001$) compared with untreated mice (**Fig. 5j; Supplementary Table 3**). DC survival was significantly increased in the middle ($P = 0.0009$) and basal ($P < 0.0001$) turns (**Fig. 5k**). Treatment also restored 9-NN distance and 9-NN CV in the apical and middle turns to levels comparable to WT, but not in the basal turn (**Supplementary Fig. 11**). Together, these findings demonstrate that base editing administered after cochlear maturation can improve auditory function and delay structural progression when treatment is initiated before the onset of overt DC disorganization.

Post-maturation base editing shifted DC-associated transcriptional programs toward a WT-like state

To define treatment-associated transcriptional changes in the context of *MPZL2* deficiency, we conducted single-cell RNA sequencing (scRNA-seq) on cochleae from 6-week-old FL-*hMPZL2*$^{WT/WT}$, untreated FL-*hMPZL2*$^{Q74X/Q74X}$, and treated FL-*hMPZL2*$^{Q74X/Q74X}$ mice. In FL-*hMPZL2*$^{WT/WT}$ cochleae, human *MPZL2* transcripts were detected predominantly in the organ of Corti and lateral-wall cell populations, consistent with previous cochlear scRNA-seq datasets[7,39,40]. These transcripts were markedly depleted in the corresponding populations of FL-*hMPZL2*$^{Q74X/Q74X}$ cochleae; however, these transcripts became detectable again in the organ of Corti populations following treatment, most notably in DCs (**Fig. 5l–m and Supplementary Fig. 12**). We next examined treatment-associated transcriptional changes in DCs. Pairwise expression analysis identified 584 genes with higher expression in FL-*hMPZL2*$^{WT/WT}$ versus FL-*hMPZL2*$^{Q74X/Q74X}$ DCs and 403 genes with higher expression in treated versus untreated FL-*hMPZL2*$^{Q74X/Q74X}$ DCs (area under the curve (AUC) ≥ 0.75) **(Supplementary Table 2-3).** Of these, 133 genes overlapped between the two comparisons, thereby identifying those with treatment-associated shifts toward WT-like expression (**Fig. 5n and Supplementary Table 4)**. To place these transcriptional shifts in a broader biological context, we performed gene set enrichment analysis (GSEA) of the FL-*hMPZL2*$^{WT/WT}$ vs. FL-*hMPZL2*$^{Q74X/Q74X}$ DC comparison, which identified 73 significant biological processes (**Supplementary Fig. 13a**). Independently, in silico *Mpzl2* perturbation followed by GSEA using scTenifoldKnk[41] identified 207 pathways (**Supplementary Fig. 13b**), 36 of which overlapped with those identified experimentally (**Supplementary Fig. 13c**). These convergent pathways included processes related to known function

of *Mpzl2*, including cell–cell adhesion[42,43], actin filament-based processes[21,42,44], cell–cell signaling[44], and cell junction organization[21,42] (**Supplementary Fig. 13d–e**). Among the 133 genes showing treatment-associated shift toward WT-like expression, 40 were associated with these selected pathways (**Fig. 5o, Supplementary Table 5**). Of these, 11 genes: *Tmod1*, *Gata3*, *Gjb2*, *Syne2*, *Rhou*, *Rflnb, Nedd4*, *Nrcam, Sdc4*, *Cd9*, and *Ndfip1*—were also among the top leading-edge genes contributing to pathway enrichment (**Fig. 5p**). Together, these findings suggest that post-maturation base editing was associated with a partial shift of DC-associated transcriptional programs toward a WT-like state.

Loss of therapeutic benefit after the onset of DC disorganization despite preserved editing efficiency

We next asked whether base editing remained therapeutically effective when treatment was initiated after the onset of structural pathology. FL-*hMPZL2*$^{Q74X/Q74X}$ mice were therefore treated at P42, when DC disorganization had already emerged, but substantial DC and OHC loss had not yet occurred (**Fig. 6a**). Auditory function was assessed at 8 and 12 weeks of age, followed by targeted deep sequencing of the organ of Corti at 12 weeks. Although on-target A5 editing efficiency in cochleae harvested at 12 weeks of age reached 6.32 ± 1.06% following P42 treatment (n = 6 ears; **Fig. 6b**), P42-treated FL-*hMPZL2*$^{Q74X/Q74X}$ mice showed no improvement in ABR thresholds at any frequency tested, at either 8 or 12 weeks of age, compared with untreated littermates (**Fig. 6c–f**). DPOAE thresholds likewise showed no significant improvement at either time point, indicating no detectable recovery of OHC-dependent cochlear function. In P42-treated ears with paired ABR sequencing data, on-target A5 editing efficiency did not correlate with ABR thresholds at click, 4, 8, or 16 kHz at 12 weeks of age (Spearman ρ = -0.17, -0.24, -0.06, and -0.14, P = 0.750, 0.644, 0.933, and 0.800; **Fig. 6g**). Notably, ears with editing efficiencies as high as 9.53% still showed no threshold improvement, suggesting that the absence of therapeutic benefit following P42 treatment was unlikely to be explained by insufficient editing alone. Integrating these findings with the responses observed at P14–P15, P28–P30, and P42 (**Fig. 6h**), auditory benefit tracked the structural state of the organ of Corti rather than the level of editing achieved.

In vivo biodistribution and safety evaluation of dual AAV-ie-K558R-ABE8eWQ-SpRY:sgRNA3

To further evaluate the biodistribution and safety of the dual-AAV base-editing system, inner ear injection was performed in P14–P15 FL-*hMPZL2*$^{Q74X/Q74X}$ mice (**Fig. 7a**). At P28–30, major non-cochlear tissues, including the brain, liver, lung, kidney, and thigh muscle, were collected and analyzed by targeted deep sequencing to assess on- and off-target editing. Off-target sites previously evaluated in the cochlea were further examined across these tissues. Editing frequencies remained below 0.2% in all tissues analyzed (**Fig. 7b**). Hematoxylin and eosin (H&E) staining revealed no treatment-associated structural abnormalities in these peripheral organs (**Fig. 7c**). Consistently, caspase-3/7 activity was comparable between treated and control tissues (**Fig. 7d**), and immunoblotting likewise showed no treatment-associated increase in cleaved caspase-3 (**Supplementary Fig. 14**), indicating no detectable increase in apoptosis.

Safety evaluation in human iPSC-derived otic progenitor cells and PBMCs

We next assessed editing activity and cytotoxicity in otic progenitor cells differentiated from control GM25256 and patient-derived SNUH422-907 iPSCs (**Fig. 7e**). Otic differentiation was confirmed by expression of the lineage markers *PAX2*, *PAX8*, *DLX5*, *SIX1*, *EYA1*, and *GATA3* (**Fig. 7f**). Following exposure to the dual-AAV base-editing system at 5×10^5 genome copies per cell, targeted sequencing confirmed on-target A5 editing in SNUH422-907-derived otic progenitor cells (29.38% ± 4.91%; **Fig 7g**), and RT-PCR demonstrated recovery of the *MPZL2* transcript following treatment (**Fig. 7h**). Under the same exposure conditions, treatment did not reduce CCK-8-based cell viability or increase caspase-3/7 activity in either GM25256- or SNUH422-907-derived otic progenitor cells relative to untreated controls (**Fig. 7i**). We subsequently assessed the inflammatory response to the dual-AAV base-editing system in PBMCs from two patients carrying the *MPZL2* c.220C>T variant (SNUH1490-3144 and SNUH1459-3066) and a healthy donor (**Supplementary Fig. 15a**). PBMCs were exposed to the dual-AAV base-editing system at 5×10^5 genome copies per cell; however, this exposure did not significantly increase IL-6 or TNF-α secretion relative to untreated cells in either patient-derived or healthy control PBMCs. In contrast, lipopolysaccharide treatment at 50 or 100 ng/mL robustly increased the levels of both cytokines, confirming assay responsiveness (**Supplementary Fig. 15b**). Overall, these analyses demonstrated on-target editing and *MPZL2* transcript recovery in patient-derived otic progenitor cells without detectable cytotoxicity, and no detectable increase in IL-6 or TNF-α secretion following exposure to the dual-AAV base-editing system in human PBMCs.

Discussion

Most in vivo genome-editing studies for hereditary deafness have evaluated proof-of-concept efficacy after neonatal intervention[17], including previous AAV-mediated gene replacement[20] and adenine base editing[18] targeting *MPZL2* c.220C>T, making post-maturation efficacy and safety essential for clinical translation. Although adult-stage CRISPR–Cas9 editing has been effective in *Mir96* and *P2rx2* mouse models[45,46], whether base editing remains effective after maturation in a progressive disorder with evolving organ of Corti pathology remained unknown. Recently, postnatal AAV-mediated *SLC26A4* replacement in a DFNB4 model defined a therapeutic window spanning neonatal and juvenile stages, with treatment at P21 improving auditory thresholds into adulthood[47]. However, that study did not identify a stage at which intervention ceased to be effective, leaving unresolved whether such windows close through loss of delivery competence or irreversible tissue-level change. Therefore, we generated a full-length humanized *MPZL2* mouse model (FL-*hMPZL2*$^{Q74X/Q74X}$), better positioned to recapitulate human-specific transcript processing and regulation[48,49]. Post-maturation treatment at P28–P30 produced significant auditory recovery when hearing loss was substantial but DC architecture remained preserved. In contrast, treatment at P42 provided no clear benefit after overt DC disorganization had begun. Our data address this distinction directly: on-target editing at P42 was comparable to or exceeded that achieved at P28–P30, indicating that the therapeutic window closed despite preserved delivery and editing competence.

DCs and pillar cells extend phalangeal processes that, with OHC apical surfaces, form the reticular lamina, which the basal OHC–DC complex mechanically couples to the basilar membrane, supporting sound propagation and cochlear amplification[50,51]. Loss of *MPZL2* caused DC disorganization as the earliest structural abnormality, potentially disrupting this coupling and impairing hearing before overt cell loss. Our previous bulk RNA-sequencing analysis of P28 cochleae identified alterations in cell adhesion and extracellular matrix organization[18]. Consistently, single-cell transcriptomic profiling of P42 FL-*hMPZL2*$^{Q74X/Q74X}$ cochleae and in silico *Mpzl2* perturbation analyses in this study likewise converged on DC programs involving cell–cell adhesion and junctional organization. Accordingly, base editing initiated at P28–P30, after cochlear maturation but before DC disorganization, restored *MPZL2* expression and shifted DC-associated transcriptional programs toward a WT-like state. These treatment-associated transcriptional shifts paralleled delayed DC disorganization and preservation of DCs and OHCs histologically, together with sustained auditory improvement predominantly at low-to-mid frequencies.

Two aspects warrant further consideration: treatment at P28–P30 improved low- and mid-frequency but not high-frequency thresholds, whereas treatment at P42 conferred no benefit at any frequency. Both are explained if the cochlea continues to deteriorate during the interval between injection and effective correction, with the basal turn losing structural integrity first. Basal DCs are shorter and stiffer than their apical counterparts, and the axial and bending stiffness of their phalangeal processes increases several-fold from apex to base[52,53]. Because cochlear amplification depends on the geometry of the DC–OHC complex[50,51], an equivalent loss of *MPZL2* reaches the threshold for disorganization earliest

in the basal turn, consistent with the basal-turn 9-NN abnormalities observed at 6 weeks while apical organization remained within the WT range. However, correction is not concurrent with administration. Reconstitution of a split-intein editor requires co-transduction of both vectors, conversion of their single-stranded genomes to double-stranded templates[54,55], and accumulation of both editor fragments before *MPZL2* can be restored; in a comparable dual-AAV cochlear system, recombined transcript was detectable at 3 days, protein at 7 days, and expression plateaued at 2–4 weeks[56]. Correction initiated at P28–P30 therefore becomes effective as basal disorganization is emerging, which would account for the absence of high-frequency benefit despite preserved architecture at the time of injection. Applying the same interval to P42 treatment places effective correction after disorganization has extended from the basal to the middle turn, leaving no region in which restored *MPZL2* could act before the threshold was crossed. This failure therefore reflects tissue state rather than editing competence, although reduced transduction of basal-turn and SCs may contribute and cannot be fully excluded[57].

In conclusion, we show that in vivo base editing remains effective after cochlear maturation, restoring *MPZL2* expression and DC transcriptional programs, auditory function, and DC organization with a favorable preclinical safety profile. Once DC disorganization had emerged, treatment conferred no benefit despite editing at least as efficient as that achieved earlier. Therapeutic efficacy is therefore determined by disease state rather than by chronological age or the technical feasibility of correction. Defining that state, rather than extending the age at which editing remains possible, will be central to translating in vivo genome editing to progressive hereditary deafness. **Acknowledgements**

This research was supported by a grant of the Korea Health Technology R&D Project through the Korea Health Industry Development Institute (KHIDI), funded by the Ministry of Health & Welfare, Republic of Korea (RS-2025-02213978 to S.-Y.L.), Phase III (Postdoctoral fellowship) grant of the SPST (SNU-SNUH Physician Scientist Training) Program (S.-Y.L.), Basic Science Research Program through the National Research Foundation of Korea (NRF) funded by the Ministry of Education, Science and Technology (RS-2026-25473248 to S.-Y.L.), SNUH Kun-hee Lee Child Cancer & Rare Disease Project, Republic of Korea (26C-059-0100, 26B-015-0100 to S.-Y.L.), and SNUH Research Fund (36-2026-3050, 32-2026-3020, 800-20250298, 800-20240497, 04-2025-3080, 03-2025-0130, 03-2024-3050, and 36-2024-0010 to S.-Y.L.).

Author contributions

S.-Y.L., and S.B. jointly conceived and supervised the project. S.J., B.-H.K., Y.C., and S.-Y.L. performed the mouse generation and in vivo experiments. W.H.C., H.K., Y.Y., and J.C. performed the in vitro experiments. W.S.B., Y.C., and H.S. performed RNA sequencing and bioinformatics analysis. S.-Y.L., and S.H.J. performed the DNA sequencing and bioinformatics analysis. S.-Y.L., S.J., W.H.C., and H.K., wrote the manuscript. D.W.N., S.C., and S.B. reviewed the manuscript. All authors read and approved the final manuscript.

Data availability

The RNA-seq data generated in this study is currently undergoing deposition in the GEO database. The

accession number will be provided upon assignment. Statistical analyses and visualizations were conducted using R Version 4.2.2 and GraphPad Prism Version 9.0.2, and the corresponding code can be accessed at https://github.com/SNUH-hEARgeneLab/MPZL2-base_editing. Any additional information required to reanalyze the data reported in this paper is available from the lead contact (maru4843@hanmail.net) upon request. All other data supporting this work are included in this article, the Supplementary Information, or source data files. Source data are provided with this paper.

Competing interests

The authors declare no competing interests.

Methods

Human genetics and clinical phenotyping

Human genetic and audiological data for the in-house cohort were obtained from individuals evaluated for hereditary deafness at Seoul National University Hospital (SNUH). The study was approved by the Institutional Review Board of SNUH (IRB-H-0905-041-281), and written informed consent was obtained from participants or their legal guardians. Genetic testing was performed using a systematic multi-tiered diagnostic strategy adapted from our previously reported integrative framework for sensorineural hearing loss[58], ranging from PCR-based screening of 22 recurrent variants in 10 classical deafness genes, including *MPZL2* c.220C>T, to whole-genome sequencing (WGS). Variant pathogenicity was assessed according to ACMG/AMP guidelines[59] and genetic diagnoses were reviewed by a multidisciplinary molecular board comprising clinicians and genome scientists. Specifically for the natural-history study of *MPZL2* c.220C>T-associated hearing loss, we retrospectively analyzed audiological data from affected individuals under a separate SNUH IRB approval (IRB-H-2607-187-1764). Published and in-house audiometric data were combined, restricting the analysis to genetically confirmed patients with DFNB111 carrying the *MPZL2* c.220C>T variant. For comparison with the mouse model, human pure-tone audiograms were grouped into age ranges of 3–9, 10–19 and 20–39 years and matched to ABR data from humanized mouse models obtained at 4, 8 and 12 weeks of age, respectively. Changes in hearing threshold (ΔThreshold) were calculated relative to baseline after normalizing the three age points to 0, 0.5 and 1. Frequency ranges were categorized as low (250 and 500 Hz in humans; 4 and 8 kHz in mice), mid (1 and 2 kHz in humans; 16 kHz in mice) and high (4 and 8 kHz in humans; 24 and 32 kHz in mice). Pearson correlation coefficients and cosine similarities were calculated for the overall hearing-loss trajectory and for each frequency range.

Generation of full-length humanized *MPZL2* mice

The targeting construct was designed based on NM_005797.4. The endogenous mouse *Mpzl2* locus was replaced with an approximately 15.9-kb human genomic fragment (GRCh38 chr11:g.118252917–g.118268857) extending from approximately 5 kb upstream of the *MPZL2* translation start site to 0.5 kb downstream of the 3′ UTR and encompassing all six exons and intervening introns. The construct carried the *MPZL2* c.220C>T (p.Q74X) variant, a neomycin-resistance cassette flanked by self-deletion anchor sequences and a diphtheria toxin A cassette. Approximately 3.5-kb 5′ and 4.8-kb 3′ homology arms were incorporated. The construct was linearized with NotI (New England Biolabs), electroporated into C57BL/6 embryonic stem cells (ESCs), and selected with G418 (Sigma-Aldrich; 200 μg/m:). Resistant clones were screened by PCR and validated by Southern blotting after digestion with SacI, BsoBI or AflII (New England Biolabs) using Neo-, 5′-arm- and 3′-arm-specific probes. A validated clone was injected into C57BL/6 albino blastocysts, followed by germline transmission and removal of the Neo cassette. A corresponding humanized WT allele was generated by CRISPR–Cas9-mediated correction of c.220C>T in zygotes derived from the FL-*hMPZL2*^{Q74} line. The sgRNA AATCTACTTACAAACTACTCAGG, a WT single-stranded donor oligonucleotide and Cas9 protein (CP1812071; Macrogen) were introduced using a NEPA21 electroporator (Nepa Gene). Founders were

screened by PCR and Bpu10I digestion (New England Biolabs) and confirmed by Sanger sequencing. Routine genotyping used tail DNA isolated with the DNeasy Blood and Tissue Kits (69506; Qiagen) and EF-Taq DNA Polymerase (SEF16-R250; SolGent). Primer sequences are provided in **Supplementary Table 4**. Mice of both sexes were used and randomly assigned where applicable. All animal procedures were approved by (IACUC NO. 24-0132-S1A3(2)).

AAV vectors and split-ABE validation

The dual-AAV split-intein ABE8eWQ–SpRY:sgRNA3 system targeting *MPZL2* c.220C>T was constructed and produced largely as previously described[18], except that the AAV-ie-K558R capsid was used in place of AAV-ie. Briefly, the N-terminal vector encoded ABE8eWQ–nCas9(N)–Npu(N), whereas the C-terminal vector encoded Npu(C)–nCas9(C) together with sgRNA3. Viral plasmids were purified using NucleoBond Xtra Midi EF (740420.5; Macherey-Nagel) and separately packaged into the N- and C-terminal AAV-ie-K558R vectors by PackGene Biotech. Low-titer preparations contained 1×10^{13} vg/mL of each vector, whereas high-titer preparations contained 5×10^{13} and 5.22×10^{13} vg/mL of the N- and C-terminal vectors, respectively. AAV-ie-K558R-GFP (5×10^{13} vg/mL) was used separately to evaluate cochlear transduction. Split-ABE expression and Npu intein-mediated reconstitution were evaluated in a previously established single-cell-derived HEK293T clone homozygous for *MPZL2* c.220C>T at the endogenous locus[18]. Cells were maintained in DMEM supplemented with 10% FBS and penicillin–streptomycin at 37°C in 5% CO_2. A total of 5×10^4 cells per condition were exposed to the N-terminal vector alone, the C-terminal vector alone or both vectors at 1×10^5 or 5×10^5 genome copies per cell and harvested 5 days later. Cells were lysed in RIPA buffer, proteins were separated by SDS–PAGE and transferred to PVDF membranes, and blots were probed with an antibody recognizing the Cas9 N terminus (MA5-23519; Invitrogen), with β-actin as the loading control. Band intensities were quantified using ImageJ v.1.54d, and reconstitution efficiency was calculated as the full-length ABE8eWQ–SpRY signal divided by the combined full-length and residual N-terminal signals. On-target and bystander editing were quantified by targeted deep sequencing.

Modified posterior semicircular canal injection into the inner ear of adult mice

FL-*hMPZL2*$^{Q74X/Q74X}$ mice of both sexes were randomly assigned to experimental groups and injected at P14–15, P28–30 or P42. All procedures were conducted aseptically using autoclaved instruments disinfected with 70% ethanol. Mice were anesthetized by intraperitoneal ketamine (100 mg/kg) and xylazine (10 mg/kg) and maintained at 37 °C on a thermostatically controlled heating pad under an operating microscope (OPMI pico, ZEISS). After hair removal below the pinna with depilatory cream (ILDONG, 251627923), a 5-mm postauricular incision was made. Subcutaneous fat and muscle were bluntly dissected to expose the PSCC, and the surgical field was dried with a Kimwipe. Phosphoric acid gel (Etching Gel, DiaDent) was applied to the bony PSCC surface through a 35-gauge needle for 1 min, removed completely, and the surface was rinsed with normal saline using Cutanplast (CureSys). A glass micropipette (WPI) connected to a Nanoliter 2020 system (WPI) was advanced through the PSCC. AAV-ie-K558R-ABE8eWQ (1.5 µL per cochlea) was delivered at 7 nL/s using a MICRO2T SMARTouch Microinjection Controller (WPI). The pipette was retained in place for 30–60 s to limit reflux and then

withdrawn slowly. The injection site was covered with adjacent fat and sealed with 3M Vetbond Tissue Adhesive (IMS,1469SB) applied through a 35-gauge needle. The incision was closed using 6-0 Vicryl sutures (NB617P, Ailee) and disinfected with povidone–iodine (Gumipharm). Mice recovered on a 37 °C heating pad and were monitored until fully awake with normal balance.

Auditory testing

ABRs and DPOAEs were recorded under ketamine–xylazine anesthesia using a BioSigRZ system (Tucker-Davis Technologies). For ABR, subdermal electrodes were positioned at the vertex, mastoid and dorsal rump. Signals were filtered between 300 Hz and 3 kHz. Clicks were presented at 21 stimuli /s from 90 to 10 dB SPL in 10-dB decrements, and responses were averaged over 512 presentations. Tone bursts (2.5ms) at 4, 8, 16, 24, and 32 kHz were presented at the same rate from 90 to 20 dB SPL in 5-10 dB decrements, and responses were averaged over 265 presentations. Threshold was defined as the lowest stimulus intensity at which ABR waves I–III were reproducibly identified. DPOAEs were measured at f2 frequencies of 4, 8, 16, 24 and 32 kHz using f2/f1 = 1.2 and L1 = L2 + 10 dB. L2 was decreased from 90 to 20 dB SPL in 5-dB steps, and threshold was the lowest L2 producing a distortion product ≥5 dB above the noise floor.

Targeted deep sequencing and off-target analyses

Genomic DNA from cultured cells was prepared using extraction buffer containing 40 mM Tris (pH 8.9), 0.01% Tween-20, 0.2 mM EDTA, proteinase K and 0.002% Nonidet P-40; tissue DNA was isolated using the Easy-DNA gDNA Purification Kit (K180001; Invitrogen). Target regions were amplified by nested PCR using KOD Multi & Epi (KME-101; Toyobo), barcoded and sequenced on an Illumina MiniSeq. For in vivo analysis, organ of Corti DNA was amplified using KOD-Plus-Neo DNA Polymerase (KOD-201; Toyobo), followed by sample-specific barcoding and 150-bp paired-end sequencing on an Illumina HiSeq platform. Editing frequencies were quantified using the ABE_detector and allsub_detector pipeline (https://github.com/BaeLab/ABE_detector_SUB_detector). For cell-enriched editing analysis, cochleae collected at P28–P30 following P14–P15 treatment were dissociated and stained with APC-conjugated anti-CD326 (17-5791-82; Invitrogen; 1:100) for 15 min, followed by 3 μM FM1-43 pulse labeling for 10 s on ice. $CD326^+$ and $CD326^+/FM1\text{-}43^{high}$ populations were isolated using a BD FACS Aria sorter and subjected to targeted sequencing. Five genomic sites previously validated by GUIDE-seq and/or Cas-OFFinder[18] were examined during *in vitro* dose validation. For in vivo assessment, candidate mouse genomic sites were identified using Cas-OFFinder with up to two mismatches in the 19-nt sgRNA target sequence, excluding the additional 5′ G used for U6 transcription, and analyzed by targeted deep sequencing. For transcriptome-wide RNA off-target analysis, total RNA from P28 cochleae following P14 treatment was isolated using TRIzol and Direct-zol RNA MiniPrep Kit. Reads were aligned to GRCm39 using HISAT2(https://github.com/DaehwanKimLab/hisat2)[60], processed using SAMtools(https://www.htslib.org)[61], and A-to-I editing events were identified using REDItools2(https://github.com/BioinfoUNIBA/REDItools2)[62]; sites with read depth <50 were excluded.

Cochlear histology, immunofluorescence and quantitative image analysis

For H&E, mice were perfused with 4% paraformaldehyde (BPP-9004-001L; T&I). Cochleae were decalcified, paraffin-embedded, sectioned at 4-μm and stained with hematoxylin and eosin. For IF, cochleae were fixed overnight in 4% paraformaldehyde at 4 °C, decalcified with Rapid Decalcifier (64143-01; Electron Microscopy Sciences) for 45 min. Samples were cryoprotected sequentially in 10%, 20% and 30% sucrose, embedded in O.C.T compound (scigen, 4586), and cryosectioned at 10 μm. Sections were permeabilized with 1% Triton X-100, blocked with 4% BSA and incubated overnight with antibodies against MYO7A (1:400; PA1-936; Invitrogen), SOX2 (1:400; sc-365823; Santa Cruz Biotechnology), MPZL2 (1:300; 11787-1-AP; Proteintech) or TUBB3 (1:300; 801202; BioLegend) at 4 °C. Alexa Fluor-conjugated secondary antibodies (rabbit-Alexa Fluor 594, and mouse-Alex Fluor 488, 594) and DAPI-containing mounting medium (ab104139; Abcam) were used for visualization. The anti-MPZL2 antibody was raised against recombinant human MPZL2 (residues 1–215; GenBank accession BC017774) and is reported by the manufacturer to react with both human and mouse MPZL2. For whole-mount IF, decalcified cochleae were dissected and stained with MYO7A and SOX2. For three-dimensional DC analysis, confocal z-stacks acquired with a Leica TCS SP8 were analyzed using Imaris v.10 (Oxford Instruments). SOX2-positive nuclei were segmented using the Spots module, and mean distance to the nine nearest neighbors (9-NN) was calculated from three-dimensional centroid coordinates. 9-NN CV was calculated as SD(d9NN)/mean(d9NN) × 100 (d9NN; mean distance to the 9-NN). For each cochlear region, spot-level 9-NN values were summarized to generate one mean 9-NN distance and one 9-NN CV value per ear. Each analyzed ear was obtained from a different mouse and represented one biological replicate.

RNA analysis and nonsense-mediated mRNA decay

Total RNA was extracted from freshly dissected mouse cochleae using TRIzol (15596026; Invitrogen) and from cultured human cells using the RNeasy Mini Kit (74104; Qiagen). Complementary DNA (cDNA) was synthesized from 1 μg total RNA using oligo(dT) primers and AccuPower RT PreMix (K-2041-b; Bioneer). To assess nonsense-mediated decay (NMD), P28 FL-*hMPZL2*$^{Q74X/Q74X}$ cochleae were cultured in DMEM supplemented with 1% FBS and 1% B-27 (12587010; Gibco) and treated with 100 μg/mL cycloheximide (CHX) for 8 h at 37 °C; untreated FL-*hMPZL2*$^{Q74X/Q74X}$ and age-matched FL-*hMPZL2*$^{WT/WT}$ cochleae served as controls. SNUH422-907 iPSCs harboring homozygous *MPZL2* c.220C>T were cultured on Matrigel (354277; Corning) in StemFlex Medium (A3349401; Gibco) and treated with 80 μg/mL CHX for 6 h, with untreated SNUH422-907 and control GM25256 cells processed in parallel. Transcriptional profiling and molecular validation were conducted using three independent, assay-specific primer strategies. First, to verify full-length coding sequence integrity and exon–exon splicing fidelity, cDNA was amplified using species-specific primers spanning the 5′ and 3′ UTRs; these long amplicons were subsequently analyzed by bidirectional Sanger sequencing and aligned to human (NM_005797.4) or mouse (NM_001357727.1) references. Second, for the visual assessment of species-specific expression in vivo (e.g., in P56 mature cochleae) and general transcript recovery, semi-quantitative RT–PCR was performed using Platinum SuperFi II Green PCR Master Mix (12369050; Invitrogen) with a distinct set of diagnostic primers. Third, for precise NMD quantification in P28 cochleae and human iPSCs, quantitative real-time PCR (qRT–PCR) was executed using SYBR Green

qPCR Master Mix (RT501M; Enzynomics) with a dedicated short-amplicon primer set—completely separate from those used for sequencing and semi-quantitative analysis—to guarantee optimal amplification efficiency. To evaluate treatment-associated transcript recovery, cochleae from treated and untreated P28–P30 mice were analyzed in parallel via both semi-quantitative RT–PCR and qRT–PCR. Relative transcript abundance was normalized to internal controls (*GAPDH* for human or *Gapdh* for mouse) and expressed as fold changes relative to wild-type levels. All primer sequences used in this study are detailed in **Supplementary Table 5**.

Human iPSC-derived otic progenitor and PBMC assays

To generate iPSCs, SNUH422-907 fibroblasts (*MPZL2* c.220C>T homozygous) were reprogrammed (Stemgent mRNA Kit, 00-0076), expanded on Matrigel in NutriStem XF, and maintained in StemFlex with 10 μM Y-27632 post-passage. GM25256 served as WT control. Pluripotency and trilineage differentiation were verified (STEMdiff Kit, ST05230), and genotypes Sanger-sequenced. For otic differentiation (days 0–12), iPSCs were cultured in N2/B27-supplemented DMEM/F12 (Gibco) with 50 ng/mL FGF3 and FGF10 (R&D Systems). Lineage specification was confirmed by RT–PCR for *PAX2*, *PAX8*, *DLX5*, *SIX1*, *EYA1*, and *GATA3*. To evaluate therapeutic efficacy and safety, day 11 otic progenitors and freshly isolated PBMCs from two patients and a healthy donor were exposed to were exposed to dual AAV-ie-K558R-ABE8eWQ-SpRY:sgRNA3 at 5×10^5 genome copies per cell. Post-transduction, otic progenitors were assessed for on-target base editing efficiency, *MPZL2* mRNA recovery, cell viability (ab228554; Abcam), and caspase-3/7 activity (G8090; Promega). For immunogenicity, PBMC supernatants were harvested 24 h post-treatment and analyzed for secreted human IL-6 and TNF-α via ELISA (88-7066-88, 88-7346-88; Invitrogen), using 50 or 100 ng/mL lipopolysaccharide (LPS; L2630; Sigma-Aldrich) as a positive control. All measurements were normalized to untreated controls.

Biodistribution and in vivo safety

Following PSCC administration at P14–P15, brain, liver, lung, kidney, and thigh muscle were collected at P28–P30. Genomic DNA isolated from each tissue was analyzed by targeted sequencing to assess on-target editing and candidate off-target editing. For histopathological analysis, tissue sections were subjected to H&E staining and examined for treatment-related structural abnormalities. For biochemical analyses, tissue samples were homogenized on ice in lysis buffer containing 20 mM Tris-HCl (pH 7.5), 300 mM NaCl, 2 mM β-mercaptoethanol, and 10% glycerol. Homogenates were clarified by centrifugation, and supernatants were collected for downstream analyses. Protein concentrations were determined, and equal amounts were used across samples. Caspase-3/7 activity was measured using a caspase-3/7 cleavage assay (G8090; Promega) as a readout of executioner caspase activation. Apoptotic signaling was independently evaluated using aliquots of the same tissue lysates by immunoblotting for caspase-3 (14220S; Cell Signaling Technology) with GAPDH (sc-47724; Santa Cruz) used as a loading control.

Single-cell RNA sequencing and analysis

Cochleae were collected at P42 from FL-*hMPZL2*$^{WT/WT}$, untreated FL-*hMPZL2*$^{Q74X/Q74X}$ and treated FL-*hMPZL2*$^{Q74X/Q74X}$ mice, with three cochleae pooled per sample. Tissues were dissected in chilled Leibovitz's L-15 medium (11415064; Gibco) and digested in 500 µL L-15 containing collagenase IV (C1889; Sigma-Aldrich; 200 U/mL) and DNase I (DN25; Sigma-Aldrich; 10 KU/mL) at 37°C for 30 min, with gentle trituration every 10 min. Digestion was terminated by addition of FBS (10270-106; Gibco), and samples were mechanically dissociated, centrifuged, filtered through a 40-µm cell strainer and stained with propidium iodide. Viable cells were isolated using a BD FACS Symphony S6 and resuspended in L-15 supplemented with 5% FBS. Cells were partitioned into Gel Beads-in-emulsion using a Chromium X instrument. 3′ gene-expression libraries were generated using the GEM-X OCM 3′ Chip Kit v4 4-plex (10x Genomics) according to the manufacturer's protocol and sequenced on a NovaSeq X+ platform (Illumina) using paired-end reads. A custom reference containing the full-length human *MPZL2* sequence in addition to the mm10 mouse assembly was used for alignment with Cell Ranger v.10.1.0 using the multi pipeline. Ambient RNA was removed using CellBender v.0.3.2. Doublets were identified using scDblFinder v.1.27.6 with dbr.per1k = 0.004 and multiSampleMode = 'singleModelSplitThres'. Cells expressing 200–4,000 genes with <10% mitochondrial reads were retained. Reference-based cell-type annotation was performed using scNym v.0.4.0 with published cochlear single-cell and single-nucleus RNA-seq datasets from Jean et al. as reference data. Query and reference matrices were normalized to counts per million and log-transformed, and annotation was restricted to existing reference labels using config = 'no_new_identity'. Differential expression between experimental conditions was evaluated using the AUROC test implemented in Seurat FindMarkers. For gene set enrichment analysis (GSEA), AUC was transformed as 2 × |AUC − 0.5| and multiplied by average Log2 fold change to generate a directional ranking score. Mitochondrial and ribosomal genes were excluded. fgsea v.1.36.2 was run against Gene Ontology Biological Process gene sets using scoreType = 'pos' and 100,000 permutations. Benjamini–Hochberg-adjusted $P < 0.05$ was considered significant. Virtual *Mpzl2* perturbation was performed using scTenifoldKnk v.1.0.3 with published WT cochlear single-cell datasets from Jean et al. Mitochondrial genes, ribosomal genes, nuclear-encoded mitochondrial genes listed in MitoCarta v.3.0, and genes expressed in at least 10% of DCs were retained. Genes were ranked by differential-regulation distance Z score following virtual *Mpzl2* perturbation and subjected to GO Biological Process enrichment using the same GSEA framework.

Statistics

Statistical analyses were performed using R v.4.2.2 and GraphPad Prism v.9.0.2. Comparisons between two groups were performed using unpaired Student's *t*-tests where appropriate. Multiple-group comparisons were performed using one- or two-way ANOVA with Bonferroni multiple-comparisons correction or Kruskal–Wallis tests, as specified in the corresponding figure legends. Data are presented as mean ± SEM. For each age and cochlear turn, percentage reduction and WT normalization were calculated as 100 × (U − T)/U and 100 × (U − T)/(U − W), respectively, where U, T, and W denote untreated, treated, and WT group means. Derived percentages are point estimates; *P* values are from Bonferroni-adjusted comparisons of untransformed ear-level data. Statistical significance was defined as $*P < 0.05$, $**P < 0.01$, $***P < 0.001$, $****P < 0.0001$.

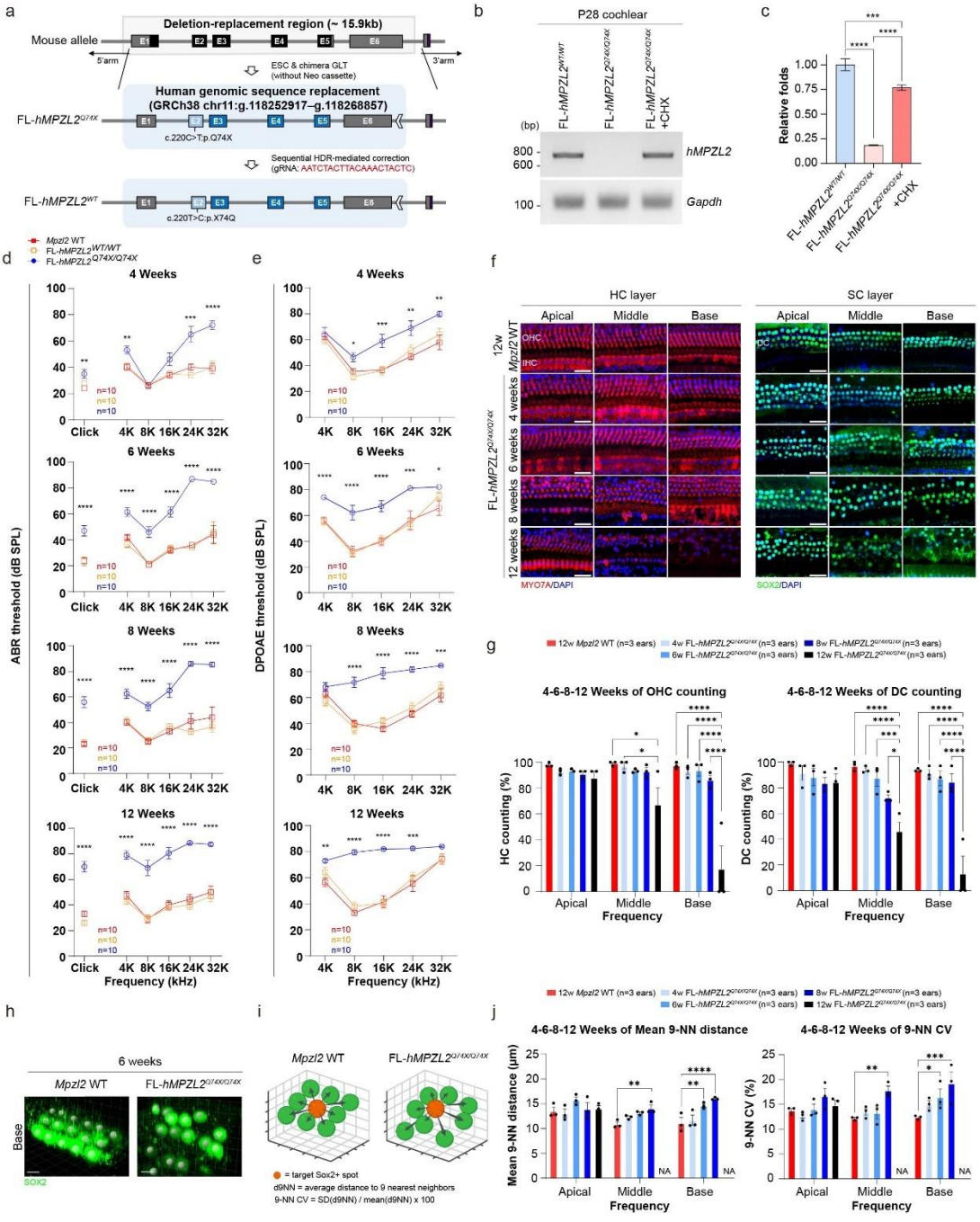

a
Deletion-replacement region (~ 15.9kb)
Mouse allele
E1 E2 E3 E4 E5 E6
5'arm
3'arm
ESC & chimera GLT
(without Neo cassette)
Human genomic sequence replacement
(GRCh38 chr11:g.118252917–g.118268857)
FL-hMPZL2Q74X
c.220C>T:p.Q74X
Sequential HDR-mediated correction
(gRNA: AATCTACTTACAAACTACTC)
FL-hMPZL2WT
c.220T>C:p.X74Q
b
P28 cochlear
FL-hMPZL2WT/WT
FL-hMPZL2Q74X/Q74X
FL-hMPZL2Q74X/Q74X +CHX
(bp)
800
600
100
hMPZL2
Gapdh
c
Relative folds
1.00
0.75
0.50
0.25
0.00
d
Mpzl2 WT
FL-hMPZL2WT/WT
FL-hMPZL2Q74X/Q74X
4 Weeks
6 Weeks
8 Weeks
12 Weeks
ABR threshold (dB SPL)
Click 4K 8K 16K 24K 32K
Frequency (kHz)
n=10
e
DPOAE threshold (dB SPL)
4K 8K 16K 24K 32K
f
HC layer
SC layer
Apical
Middle
Base
12w Mpzl2 WT
FL-hMPZL2Q74X/Q74X
4 weeks
6 weeks
8 weeks
12 weeks
OHC
IHC
DC
MYO7A/DAPI
SOX2/DAPI
g
12w Mpzl2 WT (n=3 ears)
4w FL-hMPZL2Q74X/Q74X (n=3 ears)
6w FL-hMPZL2Q74X/Q74X (n=3 ears)
8w FL-hMPZL2Q74X/Q74X (n=3 ears)
12w FL-hMPZL2Q74X/Q74X (n=3 ears)
4-6-8-12 Weeks of OHC counting
4-6-8-12 Weeks of DC counting
HC counting (%)
DC counting (%)
Apical
Middle
Base
Frequency
h
6 weeks
Mpzl2 WT
FL-hMPZL2Q74X/Q74X
Base
SOX2
i
Mpzl2 WT
FL-hMPZL2Q74X/Q74X
= target Sox2+ spot
d9NN = average distance to 9 nearest neighbors
9-NN CV = SD(d9NN) / mean(d9NN) x 100
j
4-6-8-12 Weeks of Mean 9-NN distance
4-6-8-12 Weeks of 9-NN CV
Mean 9-NN distance (μm)
9-NN CV (%)
NA
Apical
Middle
Base
Frequency

Figure 1. Generation and characterization of full-length humanized *MPZL2* mouse models.

(a) Schematic of full-length human *MPZL2* genomic replacement at the mouse *Mpzl2* locus carrying the c.220C>T (p.Q74X) variant; the FL-*hMPZL2*^{WT} allele is shown as the wild-type (WT) reference. (b–c) Representative RT-PCR (b) and quantitative RT-PCR (c) of *MPZL2* transcripts in P28 cochleae with or without cycloheximide (CHX). Expression was normalized to *Gapdh* and is shown relative to untreated FL-*hMPZL2*$^{WT/WT}$ cochleae (n = 3; mean ± standard error of the mean (SEM); one-way analysis of variance (ANOVA) with Bonferroni's multiple-comparison test; **P < 0.001; ***P < 0.0001). (d–e) Auditory brainstem response (ABR) (d) and distortion product otoacoustic emission (DPOAE) (e) thresholds in *Mpzl2* WT, FL-*hMPZL2*$^{Q74X/Q74X}$, and FL-*hMPZL2*$^{WT/WT}$ mice at 4, 6, 8, and 12 weeks (n = 10 ears per group; mean ± SEM; one-way ANOVA with Bonferroni's multiple-comparison test. *P < 0.05; **P < 0.01; ***P < 0.001; ****P < 0.0001). (f) Representative whole-mount immunofluorescent (IF) images of apical, middle, and basal turns from 12-week-old *Mpzl2* WT and 4-, 6-, 8-, and 12-week-old FL-*hMPZL2*$^{Q74X/Q74X}$ mice. MYO7A and SOX2 labeled the hair cell (HC) and supporting cell (SC), respectively. Original magnification, x80; scale bar, 25 μm. (g) Quantification of outer hair cell (OHC) and Deiters' cell (DC) numbers across cochlear turns in *Mpzl2* WT and FL-*hMPZL2*$^{Q74X/Q74X}$ mice at 4, 6, 8, and 12 weeks of age (n = 3 ears per group; mean ± SEM; two-way ANOVA with Bonferroni's multiple comparison tests. *P < 0.05; ***P < 0.001; ****P < 0.0001). (h) Representative Imaris spot overlays of SOX2-positive DC nuclei in the basal turn of 6-week-old *Mpzl2* WT and FL-*hMPZL2*$^{Q74X/Q74X}$ mice. Scale bar, 5 μm. (i) Schematic of the 9-nearest-neighbor (9-NN) analysis. For each spot, d9-NN is the mean distance to the nine nearest neighbors, and 9-NN CV is SD(d9-NN)/mean(d9-NN) × 100. (j) Quantification of mean 9-NN distance and 9-NN CV in the apical, middle and basal regions of *Mpzl2* WT and 4-, 6-, 8- and 12-week-old FL-*hMPZL2*$^{Q74X/Q74X}$ mice (n = 3 ears per group; mean ± SEM; two-way ANOVA with Bonferroni's multiple-comparisons test). Each data point represents one ear from a different mouse; thus, n also denotes the number of mice.

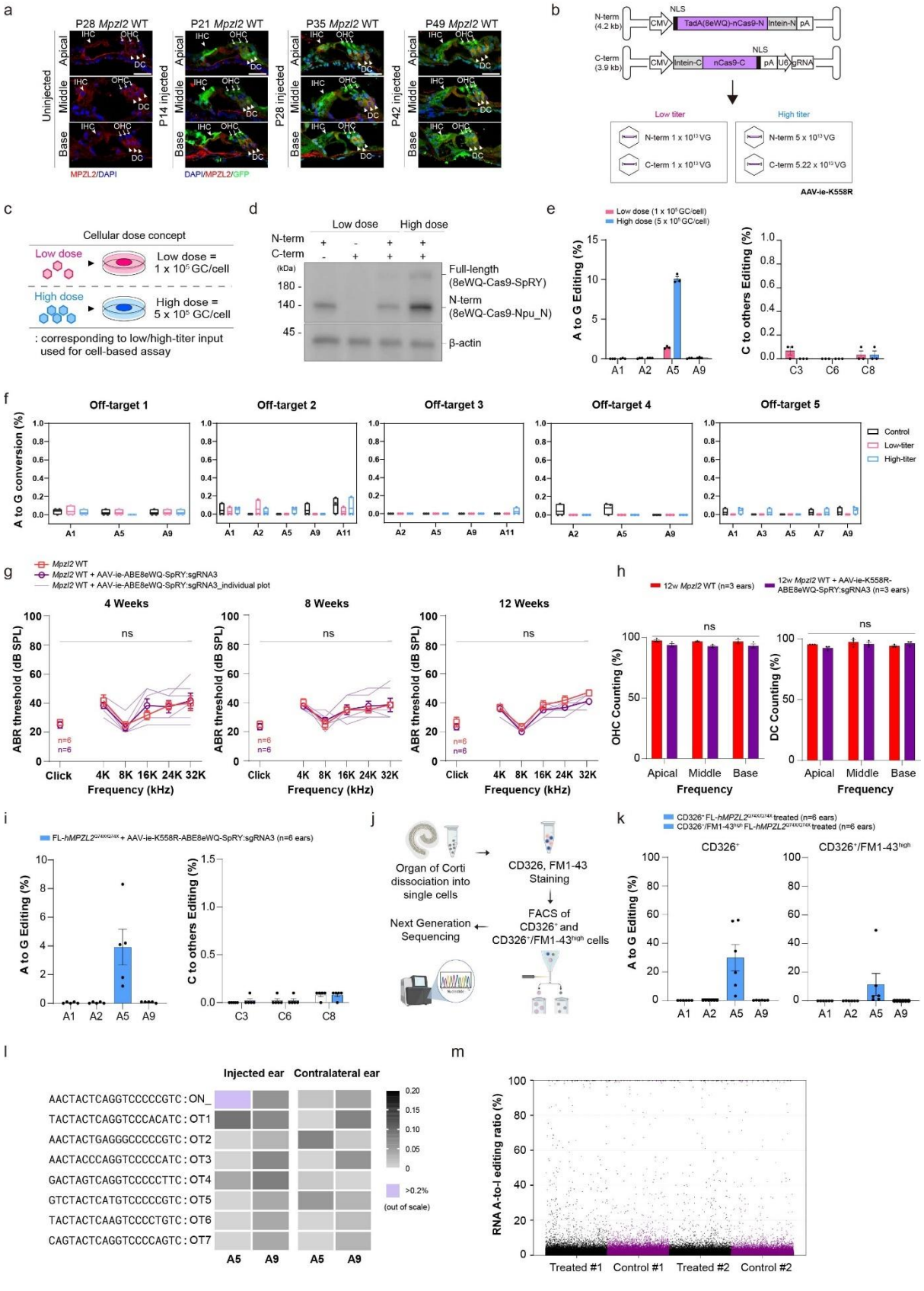
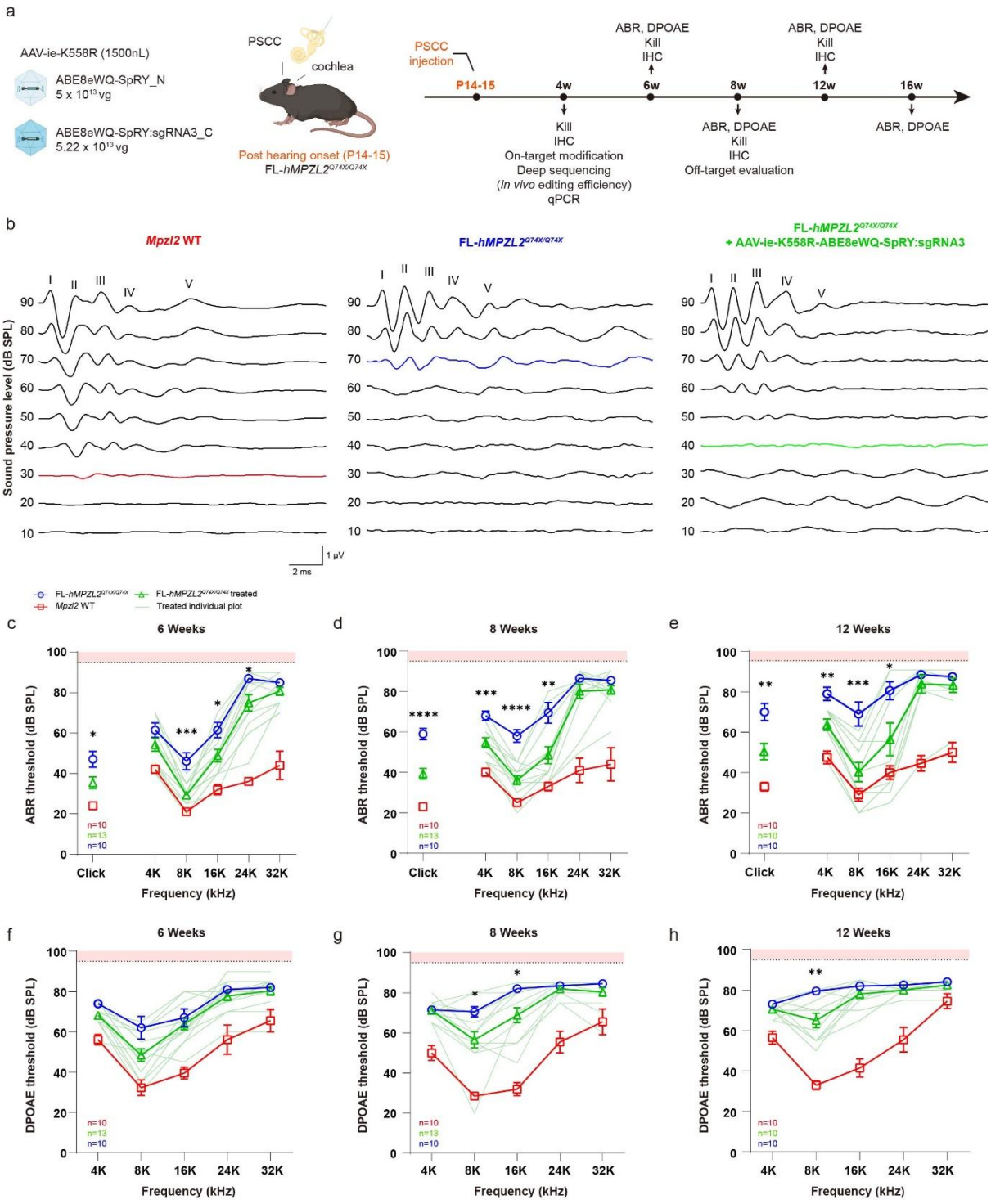

a
P28 Mpzl2 WT
P21 Mpzl2 WT
P35 Mpzl2 WT
P49 Mpzl2 WT
Uninjected
P14 injected
P28 injected
P42 injected
Apical
Middle
Base
IHC
OHC
DC
MPZL2/DAPI
DAPI/MPZL2/GFP
b
N-term (4.2 kb)
C-term (3.9 kb)
NLS
CMV
TadA(8eWQ)-nCas9-N
Intein-N
pA
Intein-C
nCas9-C
U6
gRNA
Low titer
High titer
N-term 1 x 10^13 VG
C-term 1 x 10^13 VG
N-term 5 x 10^13 VG
C-term 5.22 x 10^13 VG
AAV-ie-K558R
c
Cellular dose concept
Low dose
Low dose = 1 x 10^5 GC/cell
High dose
High dose = 5 x 10^5 GC/cell
: corresponding to low/high-titer input used for cell-based assay
d
Low dose
High dose
N-term
C-term
(kDa)
180 -
140 -
45 -
Full-length (8eWQ-Cas9-SpRY)
N-term (8eWQ-Cas9-Npu_N)
β-actin
e
Low dose (1 x 10^5 GC/cell)
High dose (5 x 10^5 GC/cell)
A to G Editing (%)
C to others Editing (%)
A1
A2
A5
A9
C3
C6
C8
f
Off-target 1
Off-target 2
Off-target 3
Off-target 4
Off-target 5
A to G conversion (%)
Control
Low-titer
High-titer
g
Mpzl2 WT
Mpzl2 WT + AAV-ie-ABE8eWQ-SpRY:sgRNA3
Mpzl2 WT + AAV-ie-ABE8eWQ-SpRY:sgRNA3_individual plot
4 Weeks
8 Weeks
12 Weeks
ABR threshold (dB SPL)
ns
n=6
Click
4K
8K
16K
24K
32K
Frequency (kHz)
h
12w Mpzl2 WT (n=3 ears)
12w Mpzl2 WT + AAV-ie-K558R-ABE8eWQ-SpRY:sgRNA3 (n=3 ears)
OHC Counting (%)
DC Counting (%)
Apical
Middle
Base
Frequency
i
FL-hMPZL2^G74XG74X + AAV-ie-K558R-ABE8eWQ-SpRY:sgRNA3 (n=6 ears)
A to G Editing (%)
C to others Editing (%)
j
Organ of Corti dissociation into single cells
CD326, FM1-43 Staining
FACS of CD326+ and CD326+/FM1-43high cells
Next Generation Sequencing
k
CD326+ FL-hMPZL2^G74XG74X treated (n=6 ears)
CD326+/FM1-43high FL-hMPZL2^G74XG74X treated (n=6 ears)
CD326+
CD326+/FM1-43high
A to G Editing (%)
l
Injected ear
Contralateral ear
AACTACTCAGGTCCCCCGTC : ON_
TACTACTCAGGTCCCACATC : OT1
AACTACTGAGGGCCCCCGTC : OT2
AACTACCCAGGTCCCCCATC : OT3
GACTAGTCAGGTCCCCCTTC : OT4
GTCTACTCATGTCCCCCGTC : OT5
TACTACTCAAGTCCCCTGTC : OT6
CAGTACTCAGGTCCCCAGTC : OT7
0.20
0.15
0.10
0.05
0
>0.2%
(out of scale)
m
RNA A-to-I editing ratio (%)
Treated #1
Control #1
Treated #2
Control #2

Figure 2. Optimization of the dual adeno-associated virus (AAV)-adenine base editing system.

(a) Mid-modiolar cryosection IF images of the AAV-ie-K558R-green fluorescent protein (GFP)–transduced organ of Corti in *Mpzl2* WT mice injected at P14, P28, and P42 and collected 7 days after injection. GFP, green; MPZL2, red; DAPI, blue. IHC, inner hair cell; OHC, outer hair cell; DC, Deiters' cell. Original magnification, x80; scale bar, 25 μm. (b) Dual-AAV vector configuration and titers. High-titer preparations contained 5×10^{13} and 5.22×10^{13} vg/mL for the N- and C-terminal vectors, respectively; and low-titer preparations contained 1×10^{13} vg/mL each. (c–d) Representative immunoblot of split-ABE expression and Npu intein-mediated reconstitution in HEK293T–*MPZL2* c.220C>T cells under low- and high-dose conditions. β-actin, loading control. (e–f) On-target and bystander editing (e) and validation of candidate off-target sites (f) after titer-dependent treatment. (g) Longitudinal ABR thresholds in untreated and dual-AAV-treated *Mpzl2* WT mice at 4, 8, and 12 weeks (n = 6 ears per group). Treated mice received 1.5 μL of dual AAV (5.11×10^{13} vg/mL) via posterior semicircular canal injection at P14–15. (h) OHC and DC numbers at 12 weeks after ABR measurement (n = 3 untreated and n = 3 treated ears; mean ± SEM). ns, not significant. (i) Targeted deep-sequencing of A-to-G at A1, A2, A5, and A9 and non-canonical cytosine editing at C3, C6, and C8 in organ of Corti collected at P28–P30 after injection at P14–P15 (n = 6 per group; mean ± SEM). (j) Schematic of fluorescence-activated cell sorting of $CD326^{+}$ and $CD326^{+}$/$FM1–43^{high}$ cochlear cells. (k) On-target editing is sorted cells from P14-treated FL-*hMPZL2*$^{Q74X/Q74X}$ mice collected at P28 (n = 6 ears). (l) Heatmap of A-to-G editing at the on-target site and seven predicted off-target sites in injected (n = 3) and contralateral cochleae (n = 2). Values >0.2% are shown separately. (m) RNA A-to-I off-target editing in 4-week-old ABE-injected and contralateral control cochleae (n = 2 each), with no substantial increase over controls. Each data point represents one ear from a different mouse; thus, n also denotes the number of mice.


a
AAV-ie-K558R (1500nL)
ABE8eWQ-SpRY_N
5 x 10^13 vg
ABE8eWQ-SpRY:sgRNA3_C
5.22 x 10^13 vg
PSCC
cochlea
Post hearing onset (P14-15)
FL-hMPZL2Q74X/Q74X
PSCC injection
P14-15
4w
6w
8w
12w
16w
ABR, DPOAE
Kill
IHC
On-target modification
Deep sequencing
(in vivo editing efficiency)
qPCR
Off-target evaluation
b
Mpzl2 WT
FL-hMPZL2Q74X/Q74X
FL-hMPZL2Q74X/Q74X
+ AAV-ie-K558R-ABE8eWQ-SpRY:sgRNA3
Sound pressure level (dB SPL)
1 μV
2 ms
Treated individual plot
c
6 Weeks
d
8 Weeks
e
12 Weeks
ABR threshold (dB SPL)
Click
4K
8K
16K
24K
32K
Frequency (kHz)
n=10
n=13
n=10
f
6 Weeks
g
8 Weeks
h
12 Weeks
DPOAE threshold (dB SPL)

731

732

Figure 3. Hearing restoration by post-hearing-onset in vivo base editing in *MPZL2* c.220C>T-associated DFNB111.

(a) Schematic of the experimental workflow for in vivo delivery of the dual-AAV adenine base-editing system via modified PSCC injection after hearing onset. (b) Representative click-evoked ABR waveforms from *Mpzl2* WT, FL-*hMPZL2*$^{Q74X/Q74X}$, and treated FL-*hMPZL2*$^{Q74X/Q74X}$ mice at 12 weeks of age. Roman numerals denote ABR waveform peaks. (c–e) ABR thresholds in *Mpzl2* WT, FL-*hMPZL2*$^{Q74X/Q74X}$, and treated FL-*hMPZL2*$^{Q74X/Q74X}$ mice at (c) 6, (d) 8, and (e) 12 weeks of age. (f–h) Corresponding DPOAE thresholds at (f) 6, (g) 8, and (h) 12 weeks of age. Data are presented as mean ± SEM; *n* values are shown in the graphs. Thin green lines indicate individual treated ears. Statistical significance was assessed using one-way ANOVA with Bonferroni's multiple-comparison test. **P* < 0.05; ****P* < 0.001; *****P* < 0.0001. Each data point represents one ear obtained from a different mouse; thus, *n* denotes the number of mice.

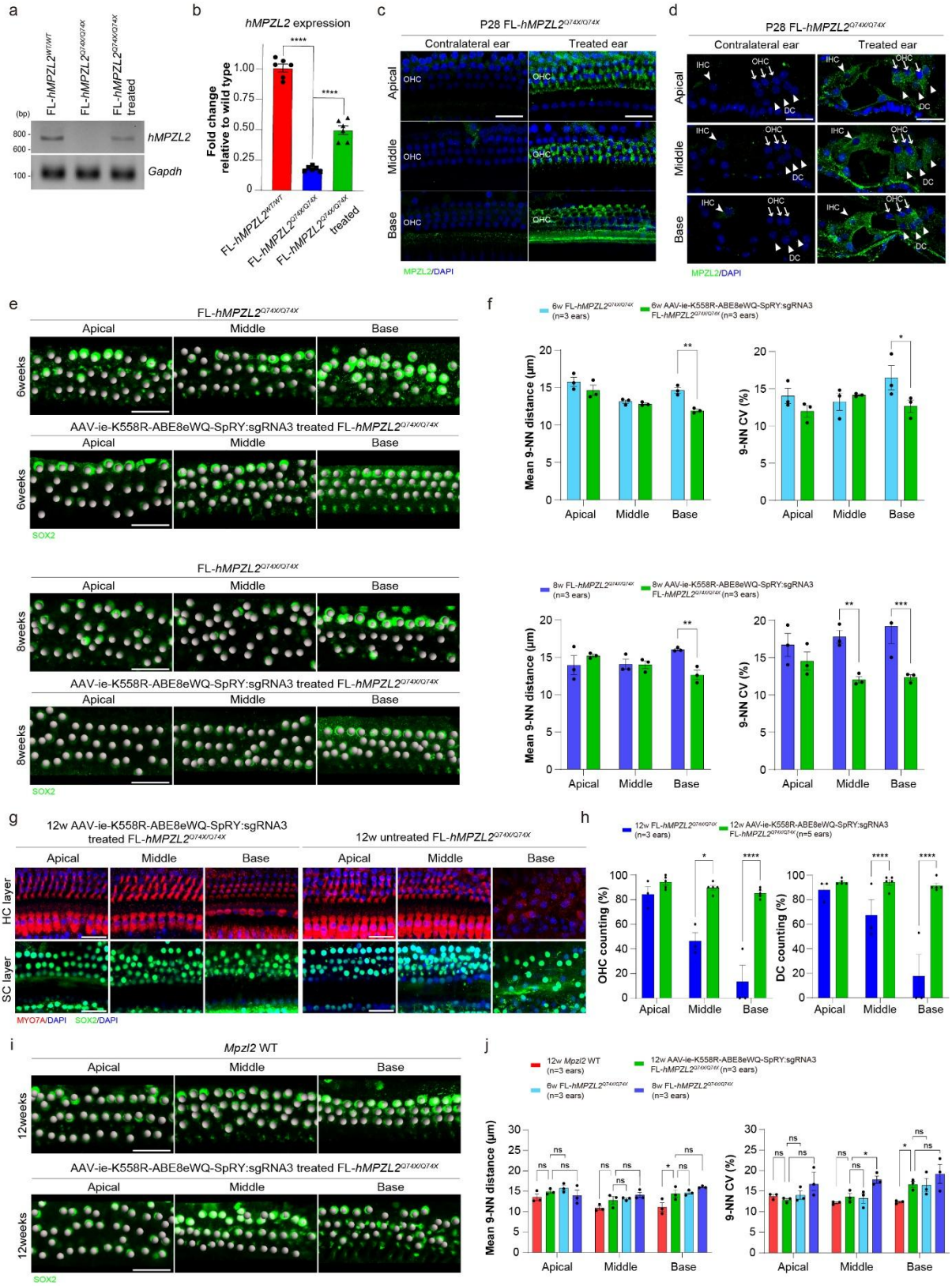

a
FL-hMPZL2WT/WT
FL-hMPZL2Q74X/Q74X
FL-hMPZL2Q74X/Q74X treated
(bp)
800
600
100
hMPZL2
Gapdh
b
hMPZL2 expression
Fold change relative to wild type
1.00
0.75
0.50
0.25
0
****
****
FL-hMPZL2WT/WT
FL-hMPZL2Q74X/Q74X
FL-hMPZL2Q74X/Q74X treated
c
P28 FL-hMPZL2Q74X/Q74X
Contralateral ear
Treated ear
Apical
Middle
Base
OHC
MPZL2/DAPI
d
P28 FL-hMPZL2Q74X/Q74X
Contralateral ear
Treated ear
IHC
OHC
DC
MPZL2/DAPI
e
FL-hMPZL2Q74X/Q74X
Apical
Middle
Base
6weeks
AAV-ie-K558R-ABE8eWQ-SpRY:sgRNA3 treated FL-hMPZL2Q74X/Q74X
SOX2
8weeks
f
6w FL-hMPZL2Q74X/Q74X (n=3 ears)
6w AAV-ie-K558R-ABE8eWQ-SpRY:sgRNA3 FL-hMPZL2Q74X/Q74X (n=3 ears)
Mean 9-NN distance (μm)
9-NN CV (%)
8w FL-hMPZL2Q74X/Q74X (n=3 ears)
8w AAV-ie-K558R-ABE8eWQ-SpRY:sgRNA3 FL-hMPZL2Q74X/Q74X (n=3 ears)
g
12w AAV-ie-K558R-ABE8eWQ-SpRY:sgRNA3 treated FL-hMPZL2Q74X/Q74X
12w untreated FL-hMPZL2Q74X/Q74X
HC layer
SC layer
MYO7A/DAPI
SOX2/DAPI
h
12w FL-hMPZL2Q74X/Q74X (n=3 ears)
12w AAV-ie-K558R-ABE8eWQ-SpRY:sgRNA3 FL-hMPZL2Q74X/Q74X (n=5 ears)
OHC counting (%)
DC counting (%)
i
Mpzl2 WT
12weeks
AAV-ie-K558R-ABE8eWQ-SpRY:sgRNA3 treated FL-hMPZL2Q74X/Q74X
SOX2
j
12w Mpzl2 WT (n=3 ears)
12w AAV-ie-K558R-ABE8eWQ-SpRY:sgRNA3 FL-hMPZL2Q74X/Q74X (n=3 ears)
6w FL-hMPZL2Q74X/Q74X (n=3 ears)
8w FL-hMPZL2Q74X/Q74X (n=3 ears)
Mean 9-NN distance (μm)
9-NN CV (%)
ns

Figure 4. Post-hearing-onset in vivo base editing restores *MPZL2* expression and preserves cochlear structure.

(a–b) Quantitative RT-PCR of *MPZL2* transcript abundance in P28–P30 cochleae from FL-*hMPZL2*$^{WT/WT}$, untreated FL-*hMPZL2*$^{Q74X/Q74X}$, and treated FL-*hMPZL2*$^{Q74X/Q74X}$ mice. Expression was normalized to *Gapdh* and is shown relative to FL-*hMPZL2*$^{WT/WT}$ cochleae (n = 3; mean ± SEM; one-way ANOVA with Bonferroni's multiple-comparison test, *P < 0.05, **P < 0.01, ***P < 0.001, and ****P < 0.0001). (c–d) Representative whole-mount (c) and cryosection (d) IF images showing MPZL2 recovery in cochleae treated at P14–P15 and harvested at P28. An anti-MPZL2 antibody (green) was used to detect MPZL2 expression. Scale bars, 25 μm. (e) Representative Imaris reconstructions show DC organization in untreated and treated FL-*hMPZL2*$^{Q74X/Q74X}$ cochleae at 6 and 8 weeks of age. (f) Quantification of mean 9-NN distance and 9-NN CV in the apical, middle, and basal regions at 6 and 8 weeks of age (n = 3 ears per group). Statistical significance was assessed using two-way ANOVA with Bonferroni multiple-comparison test. (g) Representative high-magnification (×80) whole-mount IF images of the apical, middle, and basal cochlear turns in treated FL-*hMPZL2*$^{Q74X/Q74X}$ mice. MYO7A marks the hair cell layer, and SOX2 marks supporting cells. Scale bar, 24 μm. (h) Quantification of OHC and DC numbers at 12 weeks of age (n = 5 ears). MYO7A-positive OHCs and SOX2-positive DCs were manually counted in cochlear regions corresponding to the indicated frequencies. Data are presented as the mean ± SEM. (i) Representative Imaris reconstructions show DC organization in 12-week-old *Mpzl2* WT and treated FL-*hMPZL2*$^{Q74X/Q74X}$ cochleae. (j) Quantification of mean 9-NN distance and 9-NN CV in the indicated regions of 12-week-old *Mpzl2* WT and treated FL-*hMPZL2*$^{Q74X/Q74X}$ mice, together with untreated FL-*hMPZL2*$^{Q74X/Q74X}$ mice at 6 and 8 weeks. Untreated 12-week-old FL-*hMPZL2*$^{Q74X/Q74X}$ mice were excluded from this analysis because insufficient DC numbers precluded 9-NN quantification. ns, not significant; *P < 0.05, **P < 0.01, ***P < 0.001, and ****P < 0.0001. Each data point represents one ear obtained from a different mouse; thus, n denotes the number of mice.

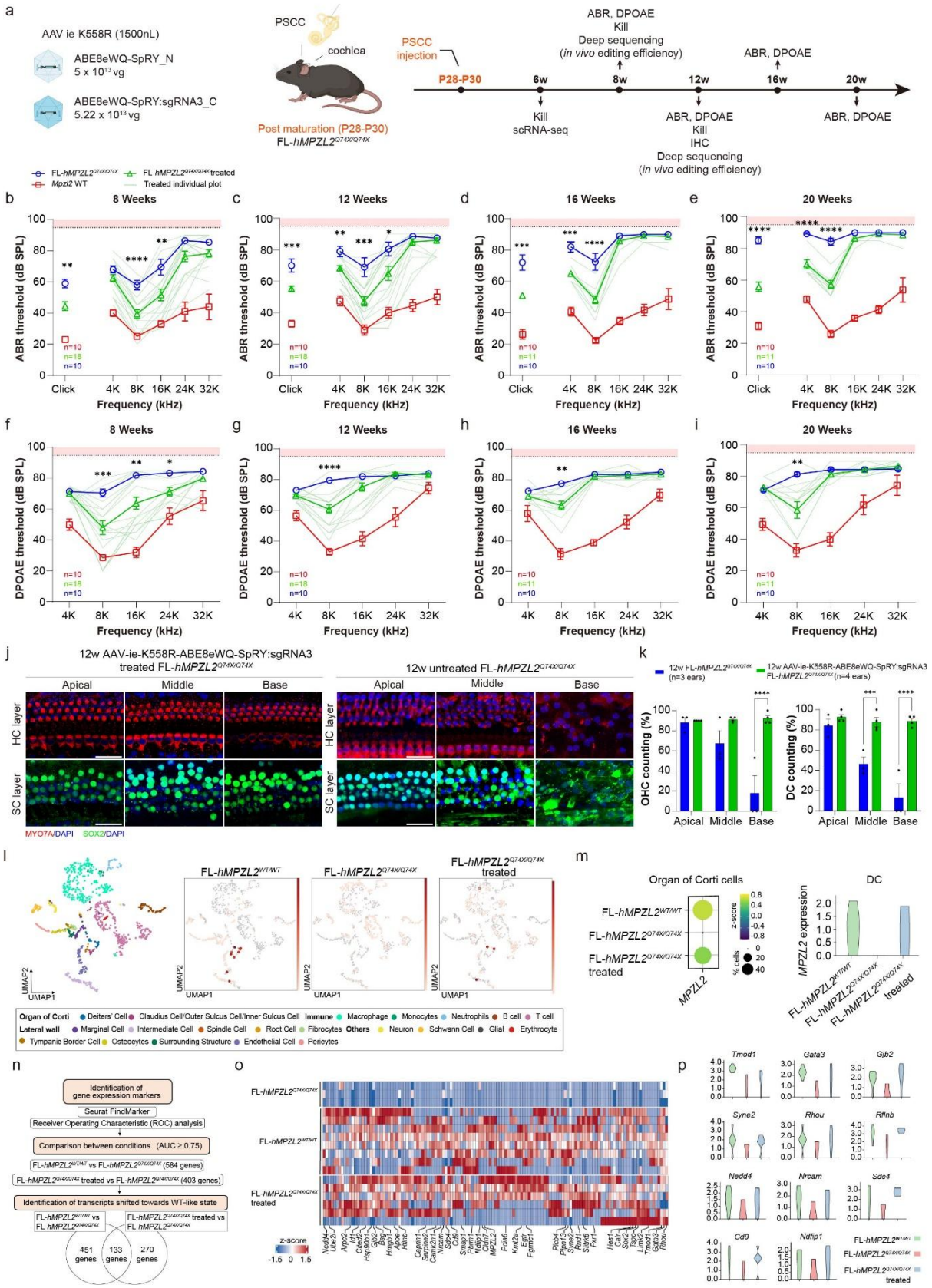

a
AAV-ie-K558R (1500nL)
ABE8eWQ-SpRY_N
5 x 10^13 vg
ABE8eWQ-SpRY:sgRNA3_C
5.22 x 10^13 vg
PSCC
cochlea
Post maturation (P28-P30)
FL-hMPZL2Q74X/Q74X
PSCC injection
P28-P30
6w
8w
12w
16w
20w
ABR, DPOAE
Kill
Deep sequencing
(in vivo editing efficiency)
Kill
scRNA-seq
ABR, DPOAE
Kill
IHC
Deep sequencing
(in vivo editing efficiency)
ABR, DPOAE
ABR, DPOAE
FL-hMPZL2Q74X/Q74X
Mpzl2 WT
FL-hMPZL2Q74X/Q74X treated
Treated individual plot
b
8 Weeks
c
12 Weeks
d
16 Weeks
e
20 Weeks
ABR threshold (dB SPL)
Click
4K
8K
16K
24K
32K
Frequency (kHz)
n=10
n=18
n=10
n=11
f
8 Weeks
g
12 Weeks
h
16 Weeks
i
20 Weeks
DPOAE threshold (dB SPL)
j
12w AAV-ie-K558R-ABE8eWQ-SpRY:sgRNA3
treated FL-hMPZL2Q74X/Q74X
12w untreated FL-hMPZL2Q74X/Q74X
Apical
Middle
Base
HC layer
SC layer
MYO7A/DAPI
SOX2/DAPI
k
12w FL-hMPZL2Q74X/Q74X (n=3 ears)
12w AAV-ie-K558R-ABE8eWQ-SpRY:sgRNA3 FL-hMPZL2Q74X/Q74X (n=4 ears)
OHC counting (%)
DC counting (%)
l
FL-hMPZL2WT/WT
FL-hMPZL2Q74X/Q74X
FL-hMPZL2Q74X/Q74X treated
UMAP1
UMAP2
Organ of Corti
Deiters' Cell
Claudius Cell/Outer Sulcus Cell/Inner Sulcus Cell
Immune
Macrophage
Monocytes
Neutrophils
B cell
T cell
Lateral wall
Marginal Cell
Intermediate Cell
Spindle Cell
Root Cell
Fibrocytes
Others
Neuron
Schwann Cell
Glial
Erythrocyte
Tympanic Border Cell
Osteocytes
Surrounding Structure
Endothelial Cell
Pericytes
m
Organ of Corti cells
DC
MPZL2 expression
z-score
% cells
n
Identification of gene expression markers
Seurat FindMarker
Receiver Operating Characteristic (ROC) analysis
Comparison between conditions (AUC ≥ 0.75)
FL-hMPZL2WT/WT vs FL-hMPZL2Q74X/Q74X (584 genes)
FL-hMPZL2Q74X/Q74X treated vs FL-hMPZL2Q74X/Q74X (403 genes)
Identification of transcripts shifted towards WT-like state
FL-hMPZL2WT/WT vs FL-hMPZL2Q74X/Q74X
FL-hMPZL2Q74X/Q74X treated vs FL-hMPZL2Q74X/Q74X
451 genes
133 genes
270 genes
o
FL-hMPZL2Q74X/Q74X
FL-hMPZL2WT/WT
FL-hMPZL2Q74X/Q74X treated
z-score
p
Tmod1
Gata3
Gjb2
Syne2
Rhou
Rflnb
Nedd4
Nrcam
Sdc4
Cd9
Ndfip1
FL-hMPZL2WT/WT
FL-hMPZL2Q74X/Q74X
FL-hMPZL2Q74X/Q74X treated

Figure 5. Post-maturation base editing restores hearing and shifts DC-associated transcriptional programs toward a WT-like state.

(a) Experimental design for post-maturation base editing and subsequent functional, histological, and transcriptomic analyses. (b–e) Age-dependent ABR thresholds in *Mpzl2* WT, FL-*hMPZL2*$^{Q74X/Q74X}$, and treated FL-*hMPZL2*$^{Q74X/Q74X}$ mice at 8 (b), 12 (c), 16 (d), and 20 (e) weeks of age. (f–i) DPOAE thresholds in the respective groups at 8 (f), 12 (g), 16 (h), and 20 (i) weeks of age. Data are presented as mean ± SEM; *n* values are indicated in the graphs. Thin green lines indicate individual treated ears. Statistical significance was determined using one-way ANOVA with Bonferroni's multiple-comparisons test. (j) Representative whole-mount IF shows HC and DC survival at 12 weeks. Representative images are stained with anti-MYO7A and anti-SOX2 antibodies. (k) Quantification of surviving OHCs and DCs. (*n* = 4 per group; mean ± SEM; statistical significance was determined using two-way ANOVA with Bonferroni multiple comparisons. ns, not significant; **P* < 0.05, ***P* < 0.01, ****P* < 0.001, and *****P* < 0.0001). (l) Global uniform manifold approximation and projection (UMAP) embedding of cochleae from FL-*hMPZL2*$^{WT/WT}$, FL-*hMPZL2*$^{Q74X/Q74X}$, and treated FL-*hMPZL2*$^{Q74X/Q74X}$ mice, colored by scNym-defined cell types. Feature plots show *MPZL2* expression for each condition. (m) Dot plot shows *MPZL2* expression in organ of Corti cells from FL-*hMPZL2*$^{WT/WT}$, FL-*hMPZL2*$^{Q74X/Q74X}$, and treated FL-*hMPZL2*$^{Q74X/Q74X}$ mice (left). Violin plot shows *MPZL2* expression across the three conditions in DCs (right). (n) Schematic of sequencing analysis to identify genes that shift toward WT-like gene expression after treatment. (o) Heatmap shows scaled expression of genes that shift toward WT-like expression after treatment, as shown in (n). 40 genes associated with cell–cell adhesion (GO:0098609), cell junction organization (GO:0034330), cell–cell signaling (GO:0007267), and actin filament-based process (GO:0030029) are labeled. (p) Violin plots show expression of genes that shift toward WT-like expression after treatment and are leading-edge contributors of FL-*hMPZL2*$^{WT/WT}$ vs. FL-*hMPZL2*$^{Q74X/Q74X}$ GSEA in cell–cell adhesion, cell junction organization, cell–cell signaling, and actin filament-based process. Each data point represents one ear obtained from a different mouse; thus, *n* denotes the number of mice.

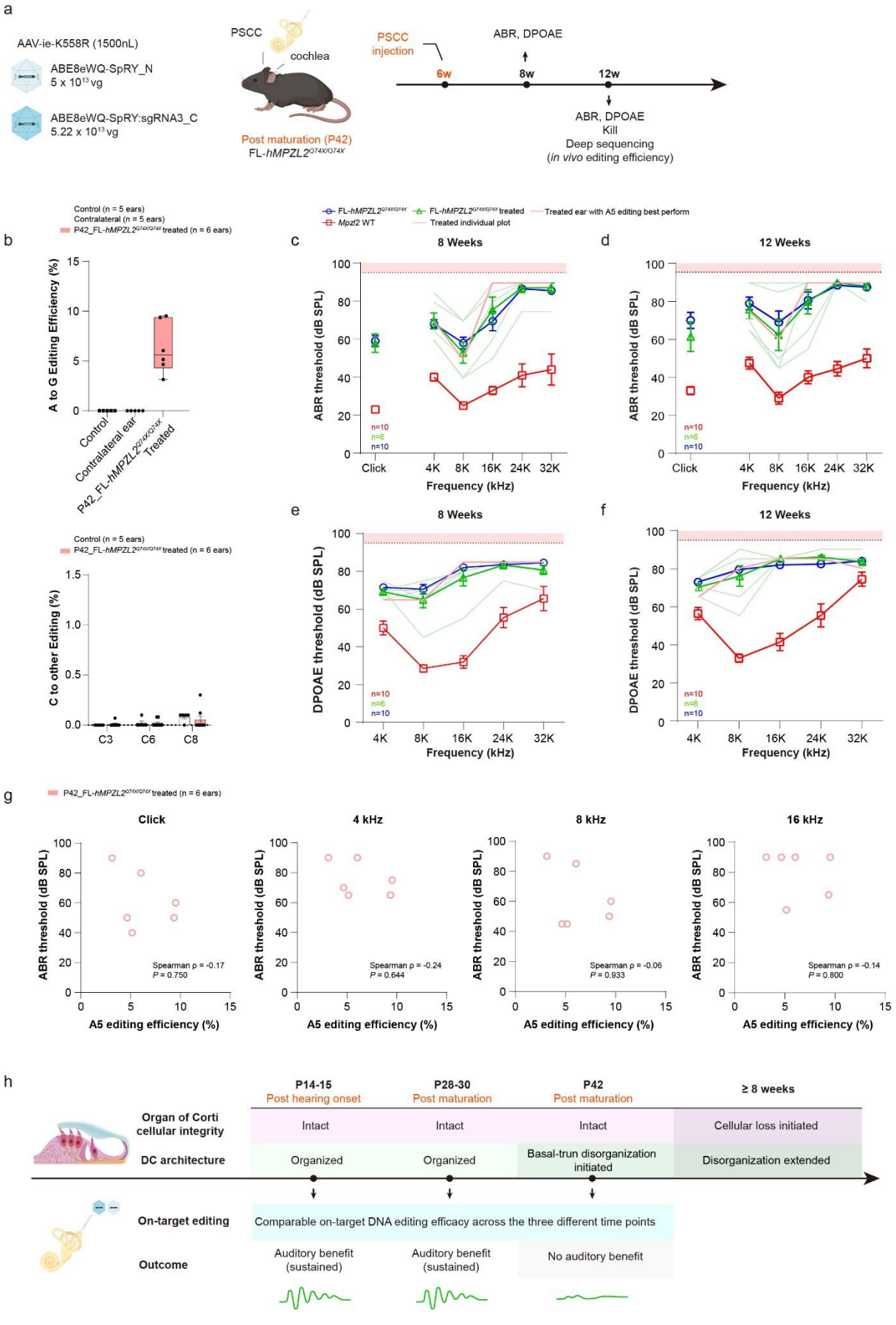

a
AAV-ie-K558R (1500nL)
ABE8eWQ-SpRY_N
5 x 10^13 vg
ABE8eWQ-SpRY:sgRNA3_C
5.22 x 10^13 vg
PSCC
cochlea
Post maturation (P42)
FL-hMPZL2Q74X/Q74X
PSCC injection
ABR, DPOAE
6w
8w
12w
ABR, DPOAE
Kill
Deep sequencing
(in vivo editing efficiency)
b
Control (n = 5 ears)
Contralateral (n = 5 ears)
P42_FL-hMPZL2Q74X/Q74X treated (n = 6 ears)
A to G Editing Efficiency (%)
Control
Contralateral ear
P42_FL-hMPZL2Q74X/Q74X Treated
C to other Editing (%)
C3
C6
C8
c
8 Weeks
d
12 Weeks
FL-hMPZL2Q74X/Q74X
FL-hMPZL2Q74X/Q74X treated
Mpzl2 WT
Treated ear with A5 editing best perform
Treated individual plot
ABR threshold (dB SPL)
DPOAE threshold (dB SPL)
n=10
n=6
n=10
Click
4K
8K
16K
24K
32K
Frequency (kHz)
e
8 Weeks
f
12 Weeks
g
P42_FL-hMPZL2Q74X/Q74X treated (n = 6 ears)
Click
4 kHz
8 kHz
16 kHz
Spearman ρ = -0.17
P = 0.750
Spearman ρ = -0.24
P = 0.644
Spearman ρ = -0.06
P = 0.933
Spearman ρ = -0.14
P = 0.800
A5 editing efficiency (%)
h
P14-15
Post hearing onset
P28-30
Post maturation
P42
Post maturation
≥ 8 weeks
Organ of Corti cellular integrity
Intact
Intact
Intact
Cellular loss initiated
DC architecture
Organized
Organized
Basal-trun disorganization initiated
Disorganization extended
On-target editing
Comparable on-target DNA editing efficacy across the three different time points
Outcome
Auditory benefit (sustained)
Auditory benefit (sustained)
No auditory benefit

Figure 6. Loss of therapeutic efficacy following P42 treatment defines a stage-dependent therapeutic window for base editing.

(a) Schematic overview of P42 treatment in FL-*hMPZL2*$^{Q74X/Q74X}$ mice, after the onset of DC disorganization but before substantial DC and OHC loss. (b) Targeted deep-sequencing of A-to-G editing at A5 (top) and non-canonical cytosine editing at C3, C6, and C8 (bottom) in organ of Corti samples at 12 weeks of age following P42 treatment (*n* = 6 ears). (c–f) ABR (c–d) and DPOAE (e–f) thresholds in *Mpzl2* WT, untreated, and P42-treated FL-*hMPZL2*$^{Q74X/Q74X}$ mice at 8 and 12 weeks. Data are mean ± SEM. Thin green lines show treated ears; the pink line indicates the ear with the highest A5 editing efficiency. (g) Correlations between A5 editing and in click, 4, 8, and 16 kHz ABR threshold at 12 weeks among P42-treated ears (*n* = 6 ears). Spearman ρ and *P* values are shown. (h) Schematic summary of cochlear structural status, on-target editing, and therapeutic outcomes following treatment at P14–P15, P28–P30, and P42. One-way ANOVA with Bonferroni's multiple-comparisons test (c–f). Each ear was obtained from a different mouse; thus, *n* denotes the number of mice.

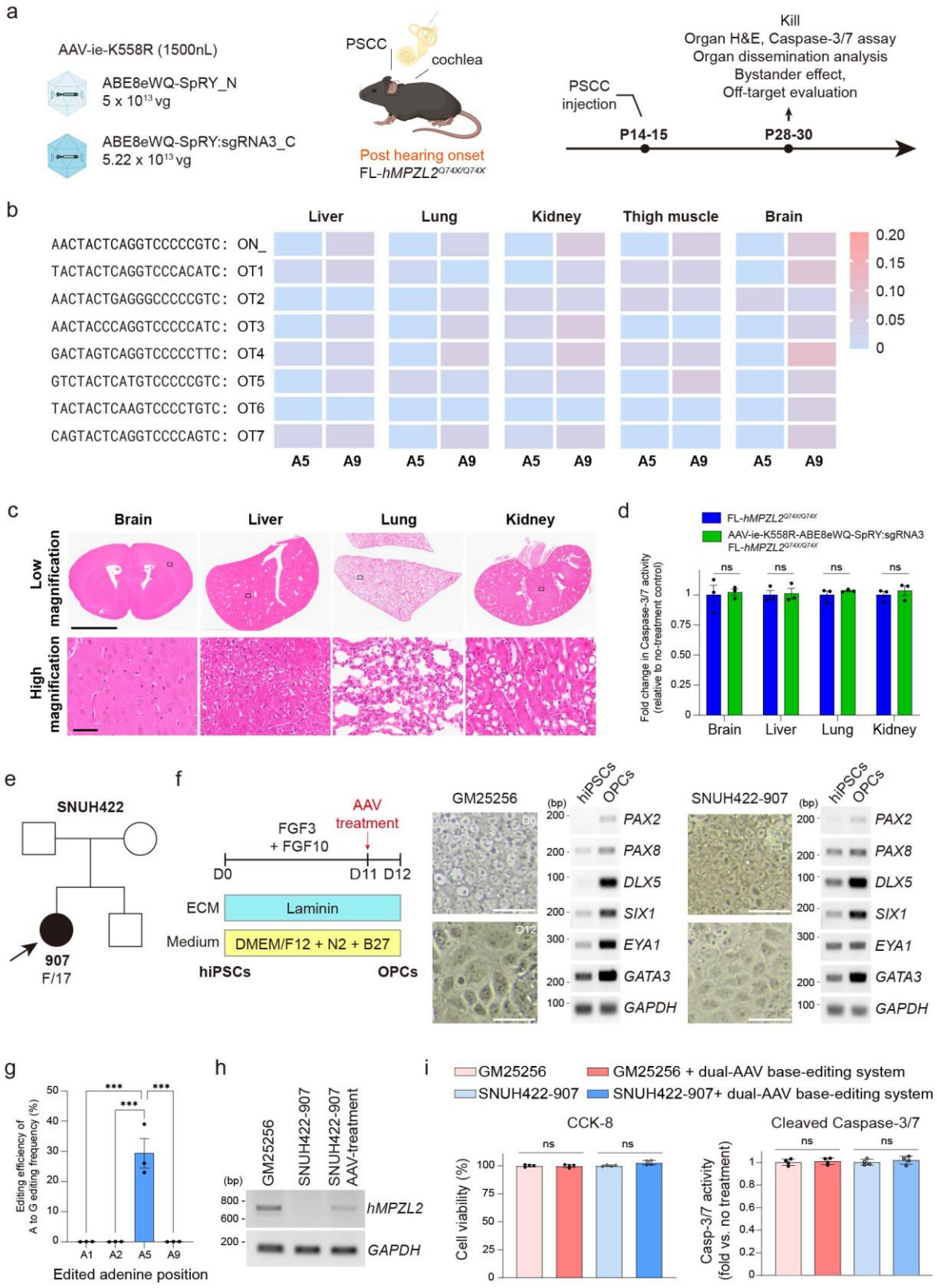

a
AAV-ie-K558R (1500nL)
ABE8eWQ-SpRY_N
5 x 10^13 vg
ABE8eWQ-SpRY:sgRNA3_C
5.22 x 10^13 vg
PSCC
cochlea
Post hearing onset
FL-hMPZL2Q74X/Q74X
Kill
Organ H&E, Caspase-3/7 assay
Organ dissemination analysis
Bystander effect,
Off-target evaluation
PSCC injection
P14-15
P28-30
b
Liver
Lung
Kidney
Thigh muscle
Brain
AACTACTCAGGTCCCCCGTC: ON_
TACTACTCAGGTCCCACATC: OT1
AACTACTGAGGGCCCCCGTC: OT2
AACTACCCAGGTCCCCCATC: OT3
GACTAGTCAGGTCCCCCTTC: OT4
GTCTACTCATGTCCCCCGTC: OT5
TACTACTCAAGTCCCCTGTC: OT6
CAGTACTCAGGTCCCCAGTC: OT7
A5
A9
0.20
0.15
0.10
0.05
0
c
Brain
Liver
Lung
Kidney
Low magnification
High magnification
d
FL-hMPZL2Q74X/Q74X
AAV-ie-K558R-ABE8eWQ-SpRY:sgRNA3
FL-hMPZL2Q74X/Q74X
Fold change in Caspase-3/7 activity (relative to no-treatment control)
ns
Brain
Liver
Lung
Kidney
e
SNUH422
907
F/17
f
AAV treatment
FGF3 + FGF10
D0
D11 D12
ECM
Laminin
Medium
DMEM/F12 + N2 + B27
hiPSCs
OPCs
GM25256
SNUH422-907
hiPSCs
OPCs
(bp)
PAX2
PAX8
DLX5
SIX1
EYA1
GATA3
GAPDH
g
Editing efficiency of A to G editing frequency (%)
***
A1
A2
A5
A9
Edited adenine position
h
GM25256
SNUH422-907
SNUH422-907 AAV-treatment
(bp)
hMPZL2
GAPDH
i
GM25256
GM25256 + dual-AAV base-editing system
SNUH422-907
SNUH422-907+ dual-AAV base-editing system
CCK-8
Cell viability (%)
ns
Cleaved Caspase-3/7
Casp-3/7 activity (fold vs. no treatment)

Figure 7. Biodistribution and safety of the dual AAV-adenine base-editing system in vivo and in patient-derived otic progenitor cells.

(a) Schematic of biodistribution and safety evaluation after inner ear injection of dual AAV-ie-K558R-ABE8eWQ-SpRY:sgRNA3 in FL-*hMPZL2*$^{Q74X/Q74X}$. (b) Heatmap of A-to-G editing frequencies at the on-target site and seven candidate off-target sites in the liver, lung, kidney, thigh muscle, and brain after PSCC administration. Editing frequencies at A5 and A9 are shown. (c) Representative hematoxylin and eosin (H&E)-stained sections of the indicated peripheral organs from untreated and AAV-treated mice collected at P28–P30 (Low-magnification images: original magnification, ×10; scale bar, 300 μm. High-magnification images: original magnification, ×40; scale bar, 50 μm). (d) Assessment of apoptosis in the indicated peripheral organs from untreated and AAV-treated mice by caspase-3/7 activity (n = 3 per group; mean ± SEM). Statistical significance was determined using two-way ANOVA with Bonferroni's multiple-comparison test; ns, not significant. (e) Pedigree of the SNUH422 family. SNUH422-907, used for induced pluripotent stem cell (iPSC) generation, is indicated by an arrow; filled symbols denote affected individuals. (f) Differentiation of control GM25256 and patient-derived SNUH422-907 iPSCs into otic progenitor cells using FGF3 and FGF10, followed by exposure to the dual-AAV base-editing system on day 11. Representative images and RT-PCR analysis of the otic lineage markers *PAX2*, *PAX8*, *DLX5*, *SIX1*, *EYA1*, and *GATA3* are shown; *GAPDH* served as a control. (g) On-target editing efficiency and *MPZL2* transcript recovery in SNUH422-907-derived otic progenitor cells following exposure to the dual-AAV base-editing system at 5 × 10^5 genome copies per cell (n = 3 per group; mean ± SEM); ***P < 0.001. (h) RT–PCR analysis of *MPZL2* transcript recovery in SNUH422-907-derived OPCs following treatment. (i) CCK-8-based cell viability and caspase-3/7 activity in GM25256- and SNUH422-907-derived otic progenitor cells after exposure to the dual-AAV base-editing system. Values were normalized to the corresponding untreated controls where indicated (n = 3 per group; mean ± SEM); ns, not significant.

References

1. Azaiez, H., *et al.* Genomic Landscape and Mutational Signatures of Deafness-Associated Genes. *Am J Hum Genet* **103**, 484-497 https://doi.org/10.1016/j.ajhg.2018.08.006 (2018).
2. Akil, O., *et al.* Dual AAV-mediated gene therapy restores hearing in a DFNB9 mouse model. *Proc Natl Acad Sci U S A* **116**, 4496-4501 https://doi.org/10.1073/pnas.1817537116 (2019).
3. Ivanchenko, M. V., *et al.* Cell-specific delivery of GJB2 restores auditory function in mouse models of DFNB1 deafness and mediates appropriate expression in NHP cochlea. *Nat Commun* **16**, 11157 https://doi.org/10.1038/s41467-025-66110-2 (2025).
4. Kim, M. A., *et al.* Gene therapy for hereditary hearing loss by SLC26A4 mutations in mice reveals distinct functional roles of pendrin in normal hearing. *Theranostics* **9**, 7184-7199 https://doi.org/10.7150/thno.38032 (2019).
5. Shubina-Oleinik, O., *et al.* Dual-vector gene therapy restores cochlear amplification and auditory sensitivity in a mouse model of DFNB16 hearing loss. *Sci Adv* **7**, eabi7629 https://doi.org/10.1126/sciadv.abi7629 (2021).
6. Pan, B., *et al.* Gene therapy restores auditory and vestibular function in a mouse model of Usher syndrome type 1c. *Nat Biotechnol* **35**, 264-272 https://doi.org/10.1038/nbt.3801 (2017).
7. Jang, S. H., *et al.* Gene supplementation with precise transgene expression rescues hearing loss in a mouse model with an Mpzl2 East Asian founder variant. *Mol Ther* **34**, 216-231 https://doi.org/10.1016/j.ymthe.2025.10.005 (2026).
8. Nist-Lund, C. A., *et al.* Improved TMC1 gene therapy restores hearing and balance in mice with genetic inner ear disorders. *Nat Commun* **10**, 236 https://doi.org/10.1038/s41467-018-08264-w (2019).
9. Valayannopoulos, V., *et al.* DB-OTO Gene Therapy for Inherited Deafness. *N Engl J Med* **394**, 1074-1083 https://doi.org/10.1056/NEJMoa2400521 (2026).
10. U.S. Food and Drug Administration. FDA Approves First-Ever Gene Therapy for Treatment of Genetic Hearing Loss Under National Priority Voucher Program.) (2026).
11. Jinek, M., *et al.* A programmable dual-RNA-guided DNA endonuclease in adaptive bacterial immunity. *Science* **337**, 816-821 https://doi.org/10.1126/science.1225829 (2012).
12. Cong, L., *et al.* Multiplex genome engineering using CRISPR/Cas systems. *Science* **339**, 819-823 https://doi.org/10.1126/science.1231143 (2013).
13. Gaudelli, N. M., *et al.* Programmable base editing of A*T to G*C in genomic DNA without DNA cleavage. *Nature* **551**, 464-471 https://doi.org/10.1038/nature24644 (2017).
14. Komor, A. C., Kim, Y. B., Packer, M. S., Zuris, J. A. & Liu, D. R. Programmable editing of a target base in genomic DNA without double-stranded DNA cleavage. *Nature* **533**, 420-424 https://doi.org/10.1038/nature17946 (2016).
15. Kosicki, M., Tomberg, K. & Bradley, A. Repair of double-strand breaks induced by CRISPR-Cas9 leads to large deletions and complex rearrangements. *Nat Biotechnol* **36**, 765-771 https://doi.org/10.1038/nbt.4192 (2018).
16. Musunuru, K., *et al.* Patient-Specific In Vivo Gene Editing to Treat a Rare Genetic Disease. *N*

Engl J Med **392**, 2235-2243 https://doi.org/10.1056/NEJMoa2504747 (2025).
17. Yeh, W. H.*, et al.* In vivo base editing restores sensory transduction and transiently improves auditory function in a mouse model of recessive deafness. *Sci Transl Med* **12**, https://doi.org/10.1126/scitranslmed.aay9101 (2020).
18. Hu, S. W.*, et al.* PAM-flexible adenine base editing rescues hearing loss in a humanized MPZL2 mouse model harboring an East Asian founder mutation. *Nat Commun* **16**, 7186 https://doi.org/10.1038/s41467-025-62562-8 (2025).
19. Ukaji, T.*, et al.* AAV-mediated base editing restores cochlear gap junction in GJB2 dominant-negative mutation-associated syndromic hearing loss model. *JCI Insight* **10**, https://doi.org/10.1172/jci.insight.185193 (2025).
20. Jiang, L.*, et al.* Hearing restoration by gene replacement therapy for a multisite-expressed gene in a mouse model of human DFNB111 deafness. *Am J Hum Genet* **111**, 2253-2264 https://doi.org/10.1016/j.ajhg.2024.08.008 (2024).
21. Wesdorp, M.*, et al.* MPZL2, Encoding the Epithelial Junctional Protein Myelin Protein Zero-like 2, Is Essential for Hearing in Man and Mouse. *Am J Hum Genet* **103**, 74-88 https://doi.org/10.1016/j.ajhg.2018.05.011 (2018).
22. Bademci, G.*, et al.* MPZL2 is a novel gene associated with autosomal recessive nonsyndromic moderate hearing loss. *Hum Genet* **137**, 479-486 https://doi.org/10.1007/s00439-018-1901-4 (2018).
23. Wang, L., Kempton, J. B. & Brigande, J. V. Gene Therapy in Mouse Models of Deafness and Balance Dysfunction. *Front Mol Neurosci* **11**, 300 https://doi.org/10.3389/fnmol.2018.00300 (2018).
24. Chang, Y. F., Imam, J. S. & Wilkinson, M. F. The nonsense-mediated decay RNA surveillance pathway. *Annu Rev Biochem* **76**, 51-74 https://doi.org/10.1146/annurev.biochem.76.050106.093909 (2007).
25. van der Valk, W. H.*, et al.* Generation and characterization of vestibular inner ear organoids from human pluripotent stem cells. *Nat Protoc* **21**, 391-428 https://doi.org/10.1038/s41596-025-01191-3 (2026).
26. Yoshida, A.*, et al.* Localization of septin proteins in the mouse cochlea. *Hear Res* **289**, 40-51 https://doi.org/10.1016/j.heares.2012.04.015 (2012).
27. Zhou, W., Jabeen, T., Sabha, S., Becker, J. & Nam, J. H. Deiters Cells Act as Mechanical Equalizers for Outer Hair Cells. *J Neurosci* **42**, 8361-8372 https://doi.org/10.1523/JNEUROSCI.2417-21.2022 (2022).
28. Jagger, D. J. & Forge, A. Compartmentalized and signal-selective gap junctional coupling in the hearing cochlea. *J Neurosci* **26**, 1260-1268 https://doi.org/10.1523/JNEUROSCI.4278-05.2006 (2006).
29. Ye, M.*, et al.* Organ of Corti macrophages: a distinct group of cochlear macrophages with potential roles in supporting cell degeneration and survival. *Front Immunol* **16**, 1617146 https://doi.org/10.3389/fimmu.2025.1617146 (2025).
30. Chu, N. T. L.*, et al.* Three-dimensional quantitative tissue clearing reveals differences in

osteovascular niche of aged and young human mesenchymal stromal cells. *Nat Biomed Eng*, https://doi.org/10.1038/s41551-026-01645-3 (2026).

31. Tao, Y.*, et al.* AAV-ie-K558R mediated cochlear gene therapy and hair cell regeneration. *Signal Transduct Target Ther* **7**, 109 https://doi.org/10.1038/s41392-022-00938-8 (2022).
32. Kim, J. & Ricci, A. J. A chemo-mechanical cochleostomy preserves hearing for the in vivo functional imaging of cochlear cells. *Nat Protoc* **18**, 1137-1154 https://doi.org/10.1038/s41596-022-00786-4 (2023).
33. Kim, J.*, et al.* Semicircular canal drug delivery safely targets the inner ear perilymphatic space. *JCI Insight* **9**, https://doi.org/10.1172/jci.insight.173052 (2024).
34. Tsai, S. Q.*, et al.* GUIDE-seq enables genome-wide profiling of off-target cleavage by CRISPR-Cas nucleases. *Nat Biotechnol* **33**, 187-197 https://doi.org/10.1038/nbt.3117 (2015).
35. Bae, S., Park, J. & Kim, J. S. Cas-OFFinder: a fast and versatile algorithm that searches for potential off-target sites of Cas9 RNA-guided endonucleases. *Bioinformatics* **30**, 1473-1475 https://doi.org/10.1093/bioinformatics/btu048 (2014).
36. Sinkkonen, S. T.*, et al.* Intrinsic regenerative potential of murine cochlear supporting cells. *Sci Rep* **1**, 26 https://doi.org/10.1038/srep00026 (2011).
37. Gale, J. E., Marcotti, W., Kennedy, H. J., Kros, C. J. & Richardson, G. P. FM1-43 dye behaves as a permeant blocker of the hair-cell mechanotransducer channel. *J Neurosci* **21**, 7013-7025 https://doi.org/10.1523/JNEUROSCI.21-18-07013.2001 (2001).
38. Landegger, L. D.*, et al.* The rise of cochlear gene therapy. *Mol Ther* **33**, 2343-2349 https://doi.org/10.1016/j.ymthe.2024.11.012 (2025).
39. Jean, P.*, et al.* Single-cell transcriptomic profiling of the mouse cochlea: An atlas for targeted therapies. *Proc Natl Acad Sci U S A* **120**, e2221744120 https://doi.org/10.1073/pnas.2221744120 (2023).
40. Sun, G.*, et al.* Single-cell transcriptomic atlas of mouse cochlear aging. *Protein Cell* **14**, 180-201 https://doi.org/10.1093/procel/pwac058 (2023).
41. Osorio, D.*, et al.* scTenifoldKnk: An efficient virtual knockout tool for gene function predictions via single-cell gene regulatory network perturbation. *Patterns (N Y)* **3**, 100434 https://doi.org/10.1016/j.patter.2022.100434 (2022).
42. Ramena, G., Yin, Y., Yu, Y., Walia, V. & Elble, R. C. CLCA2 Interactor EVA1 Is Required for Mammary Epithelial Cell Differentiation. *PLoS One* **11**, e0147489 https://doi.org/10.1371/journal.pone.0147489 (2016).
43. Guttinger, M.*, et al.* Epithelial V-like antigen (EVA), a novel member of the immunoglobulin superfamily, expressed in embryonic epithelia with a potential role as homotypic adhesion molecule in thymus histogenesis. *J Cell Biol* **141**, 1061-1071 https://doi.org/10.1083/jcb.141.4.1061 (1998).
44. Wojcik, E., Carrithers, L. M. & Carrithers, M. D. Characterization of epithelial V-like antigen in human choroid plexus epithelial cells: potential role in CNS immune surveillance. *Neurosci Lett* **495**, 115-120 https://doi.org/10.1016/j.neulet.2011.03.051 (2011).
45. Zhu, W.*, et al.* Targeted genome editing restores auditory function in adult mice with progressive

hearing loss caused by a human microRNA mutation. *Sci Transl Med* **16**, eadn0689 https://doi.org/10.1126/scitranslmed.adn0689 (2024).

46. Wei, W.*, et al.* Single-dose genome editing therapy rescues auditory and vestibular functions in adult mice with DFNA41 deafness. *J Clin Invest* **135**, https://doi.org/10.1172/JCI187872 (2025).
47. Tsai, Y. H.*, et al.* Postnatal Slc26a4 gene therapy improves hearing and structural integrity in a hereditary hearing loss model. *J Clin Invest* **136**, https://doi.org/10.1172/JCI193812 (2026).
48. Zhang, W.*, et al.* Mouse genome rewriting and tailoring of three important disease loci. *Nature* **623**, 423-431 https://doi.org/10.1038/s41586-023-06675-4 (2023).
49. Taguchi, J.*, et al.* A scalable two-step genome editing strategy for generating full-length gene-humanized mice at diverse genomic loci. *Nat Commun* **17**, 356 https://doi.org/10.1038/s41467-025-67900-4 (2026).
50. Shera, C. A. & Altoe, A. Otoacoustic emissions reveal the micromechanical role of organ-of-Corti cytoarchitecture in cochlear amplification. *Proc Natl Acad Sci U S A* **120**, e2305921120 https://doi.org/10.1073/pnas.2305921120 (2023).
51. Laffon, E. & Angelini, E. On the Deiters cell contribution to the micromechanics of the organ of Corti. *Hear Res* **99**, 106-109 https://doi.org/10.1016/s0378-5955(96)00089-5 (1996).
52. Berekmeri, E., Fekete, A., Koles, L. & Zelles, T. Postnatal Development of the Subcellular Structures and Purinergic Signaling of Deiters' Cells along the Tonotopic Axis of the Cochlea. *Cells* **8**, https://doi.org/10.3390/cells8101266 (2019).
53. Zetes, D. E., Tolomeo, J. A. & Holley, M. C. Structure and mechanics of supporting cells in the guinea pig organ of Corti. *PLoS One* **7**, e49338 https://doi.org/10.1371/journal.pone.0049338 (2012).
54. Ferrari, F. K., Samulski, T., Shenk, T. & Samulski, R. J. Second-strand synthesis is a rate-limiting step for efficient transduction by recombinant adeno-associated virus vectors. *J Virol* **70**, 3227-3234 https://doi.org/10.1128/JVI.70.5.3227-3234.1996 (1996).
55. Casey, G.*, et al.* Self-complementarity in adeno-associated virus enhances transduction and gene expression in mouse cochlear tissues. *PLoS One* **15**, e0242599 https://doi.org/10.1371/journal.pone.0242599 (2020).
56. Sellon, J. B.*, et al.* Recovery kinetics of dual AAV-mediated human otoferlin expression. *Front Mol Neurosci* **17**, 1376128 https://doi.org/10.3389/fnmol.2024.1376128 (2024).
57. Andres-Mateos, E.*, et al.* Choice of vector and surgical approach enables efficient cochlear gene transfer in nonhuman primate. *Nat Commun* **13**, 1359 https://doi.org/10.1038/s41467-022-28969-3 (2022).
58. Lee, S. Y.*, et al.* Comprehensive genetic profiling of sensorineural hearing loss using an integrative diagnostic approach. *Cell Rep Med* **6**, 102206 https://doi.org/10.1016/j.xcrm.2025.102206 (2025).
59. Oza, A. M.*, et al.* Expert specification of the ACMG/AMP variant interpretation guidelines for genetic hearing loss. *Hum Mutat* **39**, 1593-1613 https://doi.org/10.1002/humu.23630 (2018).
60. Kim, D., Paggi, J. M., Park, C., Bennett, C. & Salzberg, S. L. Graph-based genome alignment

and genotyping with HISAT2 and HISAT-genotype. *Nat Biotechnol* **37**, 907-915 https://doi.org/10.1038/s41587-019-0201-4 (2019).

61. Danecek, P.*, et al.* Twelve years of SAMtools and BCFtools. *Gigascience* **10**, https://doi.org/10.1093/gigascience/giab008 (2021).

62. Flati, T.*, et al.* HPC-REDItools: a novel HPC-aware tool for improved large scale RNA-editing analysis. *BMC Bioinformatics* **21**, 353 https://doi.org/10.1186/s12859-020-03562-x (2020).

Supplementary Files

This is a list of supplementary files associated with this preprint. Click to download.

- SupplementaryData1.xlsx
- SupplementaryData2.xlsx
- SupplementaryData3.xlsx
- SupplementaryData4.xlsx
- SupplementaryData5.xlsx
- SupplementaryMovie1.mp4
- SupplementaryTable.xlsx
- Supplementaryinformation.pdf